UNIVERSITY OF CALIFORNIA SAN DIEGO

SiC/SiC Fiber-Reinforced Composites: The Effect of Processing, Mechanical Properties, and Phase Transformation

A Thesis submitted in partial satisfaction of the requirements

for the degree Master of Science

in

Materials Science and Engineering

By

Uriel Santoro

Committee in charge:

Professor Olivia A. Graeve, Chair
Professor Javier E. Garay
Professor Marc A. Meyers

2018

The Thesis of Uriel Santoro is approved, and it is acceptable in quality and form for publication on microfilm and electronically:

_____

_____

_____

Chair

University of California San Diego

2018

Dedication

This work is dedicated to my parents; my Dad who always support me on my decisions and my Mother, who taught me to think, to listen and learn. You are the most dedicated, patience and hardworking person I know. I owe you everything.

To my Cosi; you were always there to back me up on all my choices, you are my best friend and the most perfect life partner. You truly make me a better person.

To my friends: Kike and Fernando for all the years of studying together, for always helping me with characterization, discussions, and the excellent momazos. As well to Dr. Teresita for being my second mother, always providing advice and care with a positive attitude.

To the rest of my family; Nenita and Tio Ruben who made a great effort to help me at the beginning of this journey.

Thanks.

Table of Contents

List of Tables

List of Figures

Acknowledgements

Special thanks to all the people that collaborated on the deveoplment of this study, Dr. Tarah Naoe Sullivan for all her work and help on the mechanical characterization, Dr. Keyur Karandikar for his help on the SPS sintering, Dr. Hesham E. Khalifa for providing the raw materials and HP sintering and Dr. Ekaterina Novitskaya for all her dedication, help in processing, taking micrographs and discussion.

This project was funded by the Department of Energy (grant # DE-NE0008323) through the Advanced Reactor Concepts Program. This report was prepared as an account of work sponsored by an agency of the United States Government. Neither the United States Government nor any agency thereof, nor any of their employees, makes any warranty, express or implied, or assumes any legal liability or responsibility for the accuracy, completeness, or usefulness of any information, apparatus, product, or process disclosed, or represents that its use would not infringe privately owned rights. Reference herein to any specific commercial product, process, or service by trade name, trademark, manufacturer, or otherwise does not necessarily constitute or imply its endorsement, recommendation, or favoring by the United States Government or any agency thereof. The views and opinions of authors expressed herein do not necessarily state or reflect those of the United States Government or any agency thereof.

We acknowledge the use of the UC San Diego Cryo-Electron Microscopy Facility which is supported by NIH grants to Dr. Timothy S. Baker and a gift from the Agouron Institute to UC San Diego. The SEM work was performed at the San Diego Nanotechnology Infrastructure (SDNI) of UC San Diego, a member of the National

Nanotechnology Coordinated Infrastructure, which is supported by the National Science Foundation (Grant ECCS-1542148).

ABSTRACT OF THE THESIS

SiC/SiC Fiber-Reinforced Composites: The Effect of Processing, Mechanical Properties, and Phase Transformation

By

Uriel Santoro

Master of Science

In

Material Science and Engineering

University of California San Diego, 2018

Professor Olivia A. Graeve, Chair

We describe the phase stability and suppressed β→α phase transformation in SiC/SiC fiber-reinforced composites prepared by spark plasma sintering (SPS), resulting in samples of >96% relative density and uniform β-SiC microstructure. These samples are compared to ones produced by a hot pressing (HP) technique that results in samples with ~80% conversion

to α-SiC hexagonal phases (4H and 6H). The phase transformation in the samples manufactured by SPS is shown to be significantly retarded due to the influence of lower sintering temperature, shorter processing time, and higher pressure. In addition, these samples exhibited hardness values in the range of 22 to 26 GPa, which were higher than those produced by HP, due to the higher density of the SPS samples, as well as relevant differences in phase composition. It was demonstrated that the β→α phase transformation is independent of fiber content in the composites. This study is of special interest for the production of SiC/SiC composite structures for electronic, structural and nuclear applications.

1. Introduction

1.1. Silicon Carbide

Silicon Carbide (SiC) is a ceramic material containing silicon and carbon, also known as carborundum. It can be present as a mineral called moissanite or as the synthetic form witch the first studies were performed by Jöns Berzelius in 1824 [1], at that time the properties of this material were not understood. Eugene Acherson first achieved the growth of SiC polycrystalline material using electric furnace in 1885 [2]. He was the first to recognize it as silicide of carbon and defined the chemical formula as SiC. SiC is found in nature in the form of meteorites. Therefore, SiC cannot be obtained by mining; it can only be manufactured by elaborate furnace techniques.

There are more than 250 crystalline structures of SiC [3]. SiC is recognized for having a large family of similar crystalline forms called polytypes, which are variations in crystal forms of the same chemical compound. Polymorphism is defined as a three-dimensional change by an alteration of the crystal structure or a variation in the bond angles. Polytypism is a distinct kind of polymorphism, which can occur in compounds with specific close-packed structures: on SiC only two dimensions of the unit cell remain constant for each crystal structure, while the third dimension of the crystal can change perpendicular to the planes achieving a higher density or close packing of atoms [4]. Many of the polycrystalline forms of SiC have proven to be excellent materials for high temperature, high strength, and abrasion resistant applications. The structural unit cell of all SiC polytypes is a covalently bonded tetrahedron of four Carbon atoms with one Silicon atom at the center. Each Carbon atom is surrounded by four Silicon atoms as presented in **Figure 1**, with the tetragonal bonding of a Si with the four nearest

Carbon neighbors, presenting a 120° angle between each other with a 4.36 Å lattice distance and 1.89 Å bond length [5]. The covalent bonding between silicon and carbon makes SiC a covalent ceramic rather than an ionic ceramic. Contrasting from ionic bonding, covalent bonding happens by the distribution of electrons between atoms in a lattice. A schematic of this sharing behavior in a covalent molecule can be viewed in **Figure 1**. The tetrahedra structure is linked through the corners. It is common to use a polytype notation with the letters C, H and R, which represent cubic, hexagonal and rhombohedral structure, respectively, and the numerals that represent the closet packed layers in the repeating unit. The most common polytypes are 3C ,6H , 4H and 2H; the rest of the polytypes is a mixture of these basic sequences. The only cubic polytype (3C-SiC) is also referred as β-SiC. The most common polytypes are presented in **Figure 2**.

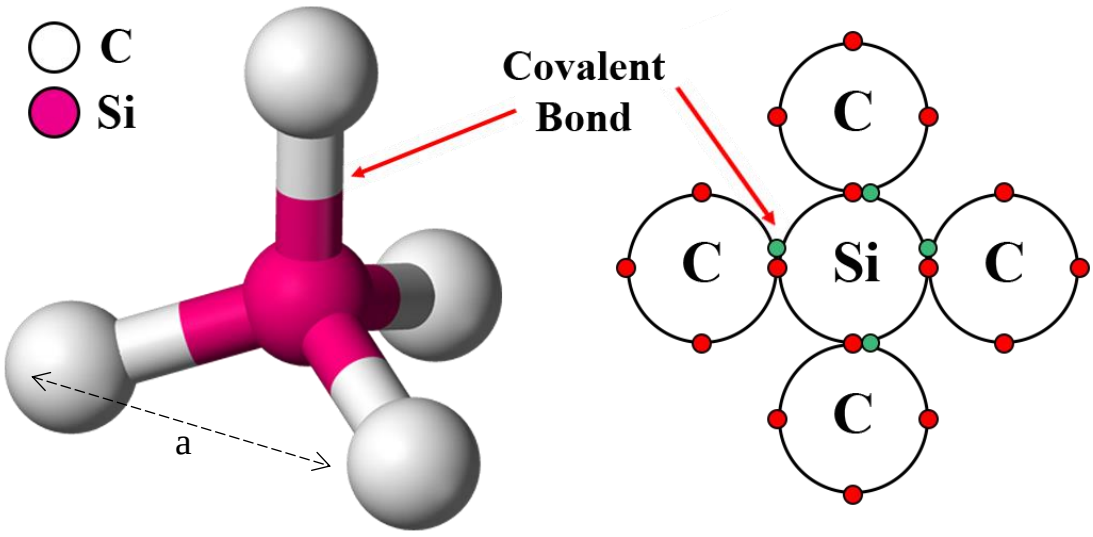

Figure 1. Silicon Carbide structure and network compound.

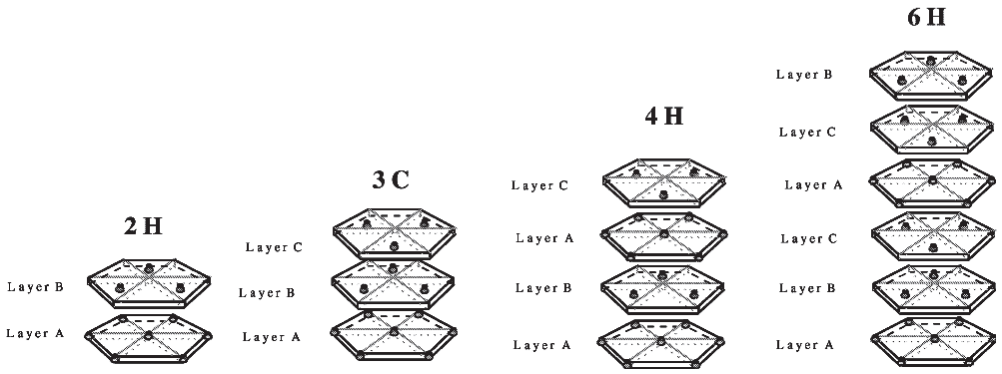

Figure 2. Representation of the most common SiC Polytypes[6].

There is still uncertainty about the kinetics and thermodynamics of polytype creation, growth, and stability, as well uncertainty in the mechanism that develops the periodic sequences. β-SiC is a metastable phase which can suffer a phase transformation into one of the α-polytypes, this transformation, and the resulting microstructure are actively dependent to the sintering temperature [7-8] applied pressure [9], sintering aids [10], starting polytype powder composition [11] and sintering atmosphere [12]. The phase transformation from β to α in SiC has been reported in exaggerated grain growth, coarsening and development of anisotropic α-SiC phase, which typically decrease the fracture toughness dramatically with the increasing α-SiC content [13].

The SiC presents difficulties when trying to be sintered close to the theoretical density due to its low sinterability; this is a result of the strong primary bonding between silicon and carbon atoms in the lattice as well as low self-diffusion rate [14].

SiC due to its covalent bonding exhibits superior mechanical properties, such as low bulk density, high strength and creep resistance at high temperatures [15], as well as excellent thermal, electrical, chemical and nuclear properties such as high thermal conductivity, high wear, low nuclear activation[16] and thermal shock resistance[17], high oxidation and chemical

resistance[18]. [19]. The material properties produced by the covalent nature of the bond between Si and C makes SiC one of the hardest materials behind diamond, cubic boron nitride, and boron carbide [Shinoda,1999]. Data corresponding to the density and hardness of different materials are summarized in Table 1.

Table 1. Density and Hardness values from most common refractory ceramics.

Materials	Density (gr/cm3)	Hardness range (GPa)
Diamond	3.51	68-98
Boron Nitride (Cubic)	3.4	34-49
Boron Carbide	2.52	28-34
Silicon Carbide	3.21	27-29
Aluminium oxide	3.93	14-19
Titanium Carbide	5.21	17-22
Silicon nitride	2.97	17-22
Boron Nitride	3.48	24-29

Since hardness is directly related to the unique materials' morphology, crystal structure, and defects that the material can have, it is difficult to directly compare the hardness data for different compounds. For this reason, the hardness values in Table 1 are presented as a range of values.

Due to its great mechanical properties in harsh environments, SiC is used in structural and mechanical applications [Vassen, 1996]. Some of these applications include cutting tools, high-temperature gas turbines, H_2 generation plants, and armor applications that take benefit from other than mechanical properties include thermal barrier coatings for aerospace applications and aeronautical [Maitre,2008], astronomical applications as a reflective material, chemically resilient parts in cryolitic melts, SiC heating devices, and a coating layer around nuclear fuel reactors [Yamamoto, 2004]. The prime candidates to benefit from the

extreme environmental resistant properties are radar and microwave applications along with other high-power devices [Yamamoto, 2004]. due to its high-temperature wide band-gap semiconducting properties.

1.2. Spark Plasma Sintering Technology

Spark Plasma Sintering (SPS) is a fairly new sintering method that has gained much interest in the last decade due to the fact that it allows a fast densification of metallic and ceramic powders [20, 21, 22, 23, 24, 25, 26, 27, 28]. This technique also commonly known in the literature as Field Assisted Sintering Technology (FAST), Pulse Electric Current Sintering (PECS) or Current Activated Pressure Assisted Densification (CAPAD). SPS, however, remains the most commonly used designation. Differences in designation often depend on the applied current or voltage (direct current, alternating current, pulsed current, current beats, high/ low voltage, or combinations)[29]. However, a study presented in **Figure 3** by Graeve *et al.* proved that the name with the highest number of hits on the web of science database for the year 2010 & 2014 is SPS [30].

Bennet *et al.* observed greater densification of alumina by gas discharge sintering in 1968 and became the first interested in SPS technique [31]. At that moment there was no interest to this process, and for more than 20 years only a few publications related to sintering in the presence of an electric field were published. The modern established SPS process reemerged in Japan in the 1990s [14,] and now it is an indubitable alternative to conventional sintering techniques. The SPS sintering method uses a direct current pulse, while uniaxial pressure is applied to a hydraulic system. A detailed schematic of the SPS equipment can be found in **Figure 4**.

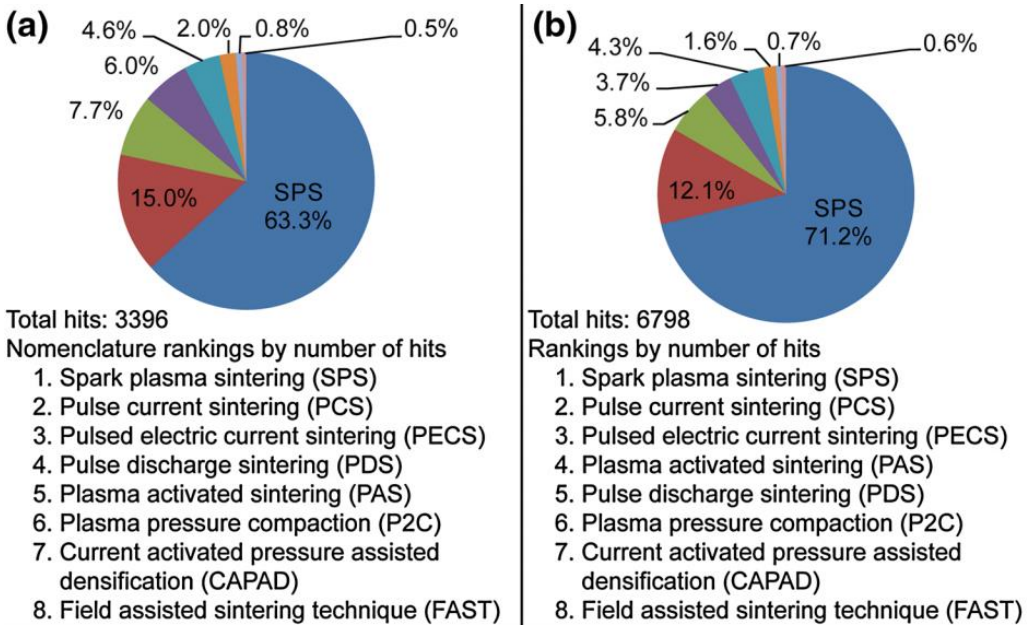

Figure 3. Web of Science statistics for spark plasma sintering up to (a) 2010 (b) 2014 [Graeve, 2015].

In the sample assembly, the surface of the graphite die is covered in graphite foil (the purpose is to protect the die and sample from reacting with each other). Another benefit is that the graphite layer is electrically conducting and soft (the purpose is to create an electrical connection between the steel pistons) the graphite die/punches and the sample, while the uniaxial pressure is applied. A schematic of the graphite dies assembly is shown in **Figure 5**.

The sample inside the graphite die is heated in two ways: internal heating caused by Joule heating and external heating when the graphite die resistively heated which then transfers a heat to the sample. Using high-density current, which is passed through the die assembly and the sample produces the heat in both cases.

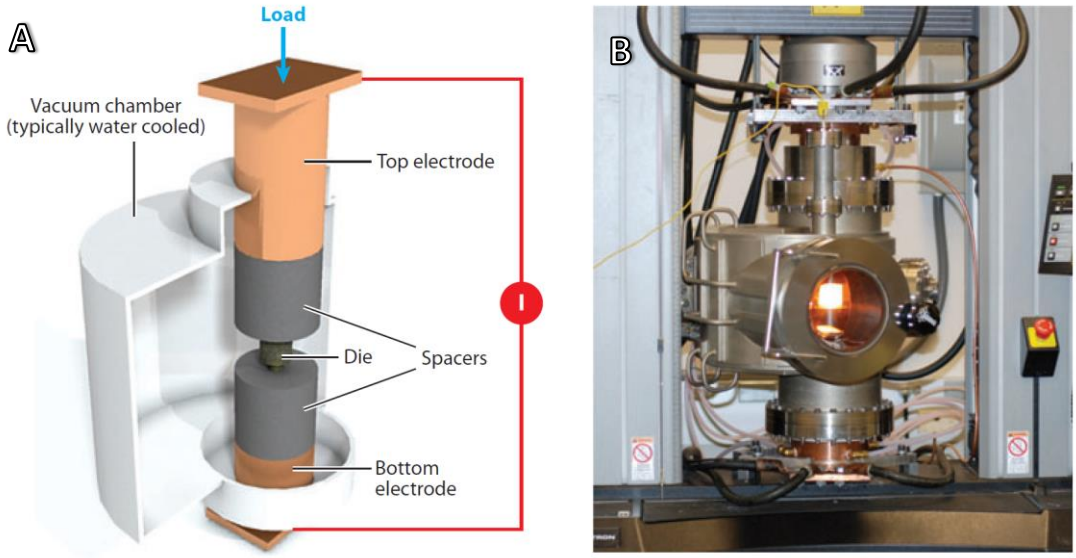

Figure 4. (a) A schematic depicting the main components of a current-activated, pressure-assisted densification (CAPAD) equipment s. (b) A picture of a CAPAD apparatus during an experiment. (Garay, 2010)

Figure 5. Graphite die assembly

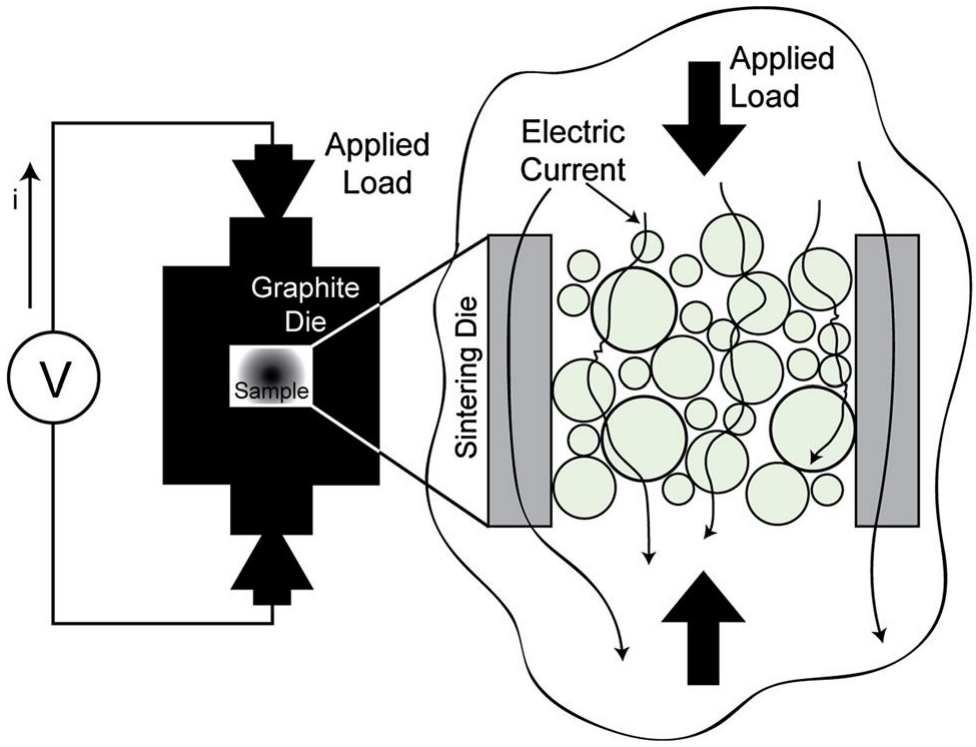

Figure 6. Sample heating produced by Joule heating and heat transfer [Graeve, 2015].

A schematic that describes the heating of the sample inside the graphite die assembly is presented in **Figure 6**. The dual heating is characteristic of the SPS sintering technique. However, sintering mechanisms occurring during SPS sintering are still not fully understood due to the complexity of the overall system.

Measuring and controlling the temperature in this process is critical to its efficiency and success. Placing an optical pyrometer on the graphite punch near the center of the powder sample is a way to control, monitor and measure the high temperatures involved in SPS sintering process. **Figure 7** demonstrates a comparison between the setup that was used in the current study (A) and the alternative setup with the pyrometer on the side (B). This setup is preferred over the alternative setup, due to a higher uniformity on the temperature. The pyrometer placed at the top of the sintering equipment unit focusing down through a hole in

the top pressure puncher looking directly to the sample. The importance of mentioning this is because some SPS equipment focuses the pyrometer on the outside of the graphite die to monitor the temperature. Vanmeensal *et al.* studied the heat distribution in an SPS unit and stated both theoretically and experimentally that the heat distributions inside a graphite die are not homogeneous [32]. However, placing the pyrometer on a hole through the top punch, rather than the outside of the graphite die could monitor the temperatures within the die more accurately. Trying to avoid temperature gradients on the sintering process is crucial to increase the reproducibility of the sintering process.

The SPS sintering technique showed outstanding efficiency on the consolidation and developing of high-density metal, and ceramic nanomaterials, composite materials, fiber reinforced matrix composites, biomedical materials, functionally gradient materials, semiconductors with thermoelectric capabilities [33 34 35 36 37].

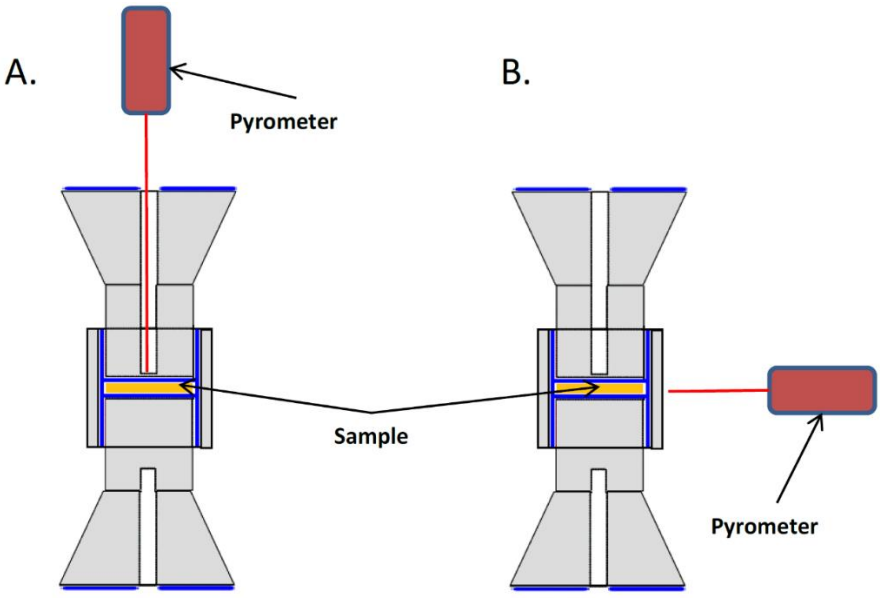

Figure 7. A schematic of the graphite die corresponding to the optical pyrometer position (A) mounted on the top, focused on the center of the sample, (B) mounted on the side, focused on the edge.

Spark Plasma Sintering remains a predominantly laboratory research stage process, with only a few exceptions that try to study the capability of the technology to be used in industry to develop products on a large scale. **Figure 8** presents potential industry applications for the SPS technology.

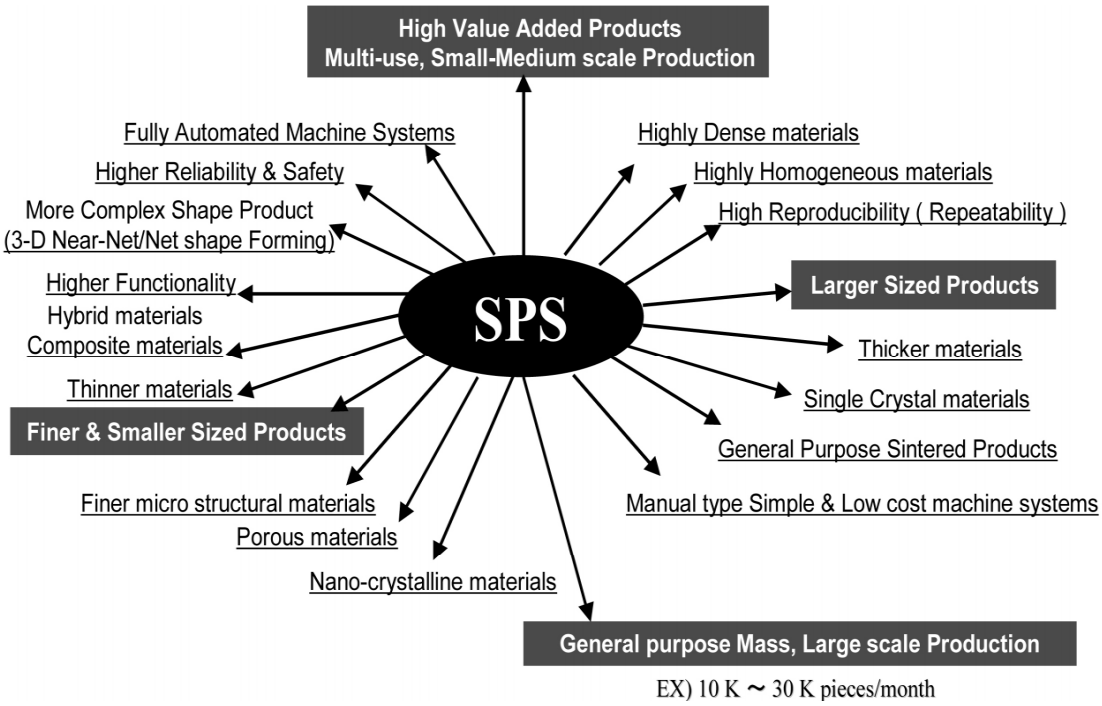

Figure 8.Different applications from industry on SPS technology [38].

There are many unique SPS's properties that can be beneficial from an industrial point of view. The main difference is the use of current along with uniaxial pressure to consolidate powder or composites. The success of this process has been possible to the clear advantages over conventional methods (e.g., Hot Press) [39]. Which includes a lower sintering temperature, faster heating rate and shorter holding time; some important features are the possible sintering of nanostructured powder close to theoretical values with minimized Ostwald ripening [40], reduced impurity segregation at grain boundaries [41], cleaner grain boundaries in sintering

ceramic materials [42] and a definite improvement of mass transfer due to the current imposition [43].

The SPS high sintering rate is achieved due to internal heating of the sample provided by Joule heating, which can provide a benefit during sintering by using elevated heating rates, avoiding the grain coarsening low-temperature mechanism, thought surface diffusion [44]. The effect of higher pressure compared to HP, influence the sintering driving force by introducing another densification mechanism like particle sliding and rearrangement contributing to the sintering. Simultaneous application of temperature and pressure can produce materials with similar or better properties than conventional sintering, leading to high-density samples, shorter sintering times, and less power consumption per sample [45].

It has been estimated that the sintering time needed to achieve 99.9% dense Ti-Al_2O_3-TiC composite by SPS is on the order of 5 minutes, while a similar density requires time on the order of 5 hours for Hot Press (HP) technique [46]. In addition, the power consumption of SPS is one third of the power needed for conventional sintering techniques like hot pressing (HP) or hot isostatic pressing (HIP) [47]. Later in this project, a more in-depth evaluation of SPS sintering and conventional HP sintering will be made to study the advantages of SPS sintering.

1.3. SiC/SiC Ceramic Matrix Composites

The major disadvantage in the performance of SiC as a ceramic material is its sensitivity to thermal and mechanical shocks [[48]]. For some applications (*i.e.*, structural, nuclear, aerospace), the brittle nature of monolithic SiC can be the cause of unacceptable safety risks. One possible solution for mitigating this major disadvantage is to design a silicon carbide fiber-silicon carbide matrix (SiC/SiC) composite, which can result in higher

toughness, and damage tolerance (*i.e.*, nonbrittle failure), caused by a deflection of the propagating crack at the boundary between the fiber and matrix [49]. With composites, designers can take advantage of the notable features of SiC, including significant high-temperature strength, high hardness, excellent corrosion resistance, high thermal conductivity, low thermal expansion and low density [50, 51, 52, 53]. Silicon carbide fiber-silicon carbide matrix (SiC/SiC) composites are an ideal candidate for next-generation nuclear reactor components, due to its ability to retain thermal and mechanical capabilities intrinsic at high-temperature [54, 55]. Furthermore, these composites have a potential for use in non-nuclear applications such as aircraft turbine engines, exhaust components, and rotors/blades [56], where high-temperature stability beyond metallic heat resistant alloys and high strengths are valued. In addition, heavier metallic alloys such as Inconel with SiC/SiC composites, a significant improvement in fuel efficiency can be achieved, due to higher SiC combustion temperature, lower component weight and reduced need for cooling [57]. SiC/SiC composite manufacturing methods include chemical vapor infiltration (CVI) [58], polymer impregnation and pyrolysis (PIP) [59], liquid silicon infiltration (LSI), as well as high-temperature techniques like hot pressing (HP) [60] or hot isostatic pressing (HIP) [61]. However, the sintered ceramic materials often suffer from a relatively high level of porosity (about 10-20%). Other drawbacks of conventional sintering techniques include the use of binders [62], sintering aids which can bring undesired reactions during sintering, as well as long processing cycles with high temperatures, increasing manufacturing costs [63].

1.4. Fiber Coatings

The interface between the matrix and fiber in the most of the CMC reside in a thin coating layer deposited on the fiber [64].

Models and experiments have been made to study the need and benefits of the interfaces in CMC and showed that a composite could be beneficial for toughness, lifetime, strength and creep resistance, especially when a strong interface is used. Not utilizing fiber coatings can yield unsatisfactory results [65] [66]. Matrix-fiber attachment is stronger in composites made of the same compound, such as SiC/SiC composites, due to their chemical similarities among fiber and matrix incline them to cohesion. However, in order to reduce their natural cohesion, a fiber coating is used.

The fiber coating is greatly valued for more than just its mechanical effects. Not only does it safeguard the fiber from when a crack extends through the matrix, but also provide thermal protection and a chemically passive barrier for the fibers. Preventing the fiber and matrix to sinter together during the process.

Other function of the coating is to isolate fibers from the neighbor, promoting a matrix to fill out in-between fibers. In composites with a strong fiber/coating bonding, the matrix cracks are dissipated through the sliding of the failed fiber segments, usually called “fiber pull-out” (cohesive failure mode) into small and branched cracks [67]. The load transfer and short debonds allow a further fracture, limiting fiber overloading during the matrix cracking. Leading to an increasing energy adsorption, which provides a damage tolerance strengthening the composite.

One of the most common methods to develop a coating in the early years of CMC development is to let the fiber and matrix species react to form a weak carbon layer as a consequence of secondary reactions during the composite manufacturing. However, the resulting composite was limited by their oxidative stability at high temperature [68]. A modern approach is to coat fibers before the composite manufacturing by the chemical vapor deposition (CVD) or liquid precursor coating methods [69]. The CVD process, brings more control of coating composition, thickness, morphology by using a gas phase precursor that reacts at the fiber surface, decomposing and forming the coating. The microstructure and properties of the coating are directly dependent on the deposition conditions [70], the thickness can range from nanometers to micrometers, which can be controlled by varying the deposition rate and time. There is a big catalogue of coating compositions that can be made by CVD, but the most common are non-oxide coatings of pyrolytic carbon (PyC) and hexagonal boron nitride (hex-BN), due to their natural capacity to be used in high temperatures without limiting the process of sintering. On this study, PyC will be used as coating for the SiC fiber as presented in **Figure 9**.

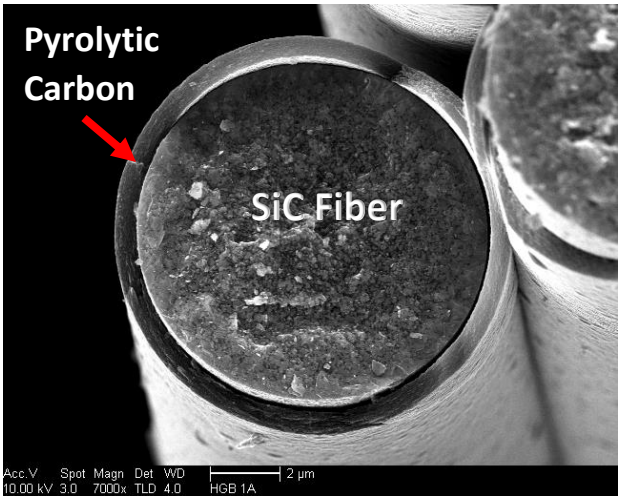

Figure 9. SEM micrograph of a SiC fiber coated with PyC by the CVD method.

1.5. SiC/SiC Ceramic Matrix Composites by SPS

One of the most frequently used material for high-temperature applications is SiC, the use of SiC ceramics brings great benefits compared to high-temperature alloys, this is due to its unique properties, such as great hardness, high strength and creep resistance in elevated temperatures, as well as high thermal conductivity and thermal shock resistance to oxidation and corrosion [71]. However, it is not commonly used as a structural material, due to its brittle nature, low fracture toughness and high flaw-crack propagation, which limits their applications [72]. To overcome these problems, a fiber reinforced SiC composites have been the center of research in recent years. SiC/SiC composite is still on the development stage, however, it shows promising future other high-end technology fields, such as aerospace and nuclear energy[34]. For example, the fracture behavior of fiber reinforced Ceramic Matrix Composites (CMC) have been studied and it is well proven that the addition of fiber reinforcement increases the flaw-sensitivity in crack deflection, fracture toughness, fiber pull-out, and crack branching effects [73]. Continuous SiC/SiC composites exhibit a ductile rupture performance similar to metals [74]. These properties are directly related to the fiber reinforcement, the interphase design and the matrix manufacture [75].

There are different methods used to manufacture reinforced CMCs. The most commonly used techniques are chemical vapor infiltration (CVI), melt infiltration (MI), polymer infiltration and pyrolysis (PIP), hot press (HP) and hot isostatic press (HIP) [28 76 77 78]. The most well-established methods used to fabricate CMCs are CVI, PIP, and MI, however, the sintered material often results in relatively high level of porosity (about 10-20%). Additionally, these processes require a long time (hours to days) with high rejection rates [79]. HP or HIP are good alternative techniques to reach a higher density of the composite as well

as mechanical properties, but both of them also require long processing cycles with high temperatures and in most cases the use of binders or oxide sintering aids.

1.6. Mechanical testing

1.6.1. Hardness

Hardness is defined as the resistance to indentation, it can also be described as the resistance to a non-recoverable deformation, fracture or densification, and is measured in units of stress (Pa, psi). Materials' deformation can be either elastic or plastic. In materials with linear elastic deformation, when the stress is applied the material starts to deform, while when the stress is removed the material will recover to its original form. The plastic deformation appears when a large load is a used to move farther than the linear elastic region, and the material is not capable of recover to its original shape [80] [81].

Hardness is measured by applying a determined load on a sharp tip to produce an indentation to the surface of the material. The measurements can be on the macro, micro, and nanoscale depending on the applied force and the size of the tip. Consequently, microhardness test acquires its name due to the small area that gets in contact with the sample. Some limitations that this technique can have are when a material has a non-homogeneous surface; it is prone to cracking or has a fine structure. Respectively, microhardness measurements are inaccurate, and cannot fully identify the surface features [82]. Hardness magnitude is calculated by the Equation 1, where the "H" is the hardness, "P" is indentation load and "a" is the projected dimension of the Vickers indenter.

$$H = \frac{P}{2a^2} \quad (1)$$

The units used in hardness are load/unit area, meaning units of pressure. Therefore, we can say that hardness is the pressure needed to make a nonrecovery plastic flow [83].

Hardness is typically used as a quality measurement to evaluate the effects of erosion, wear and machining damage [84]. The Vickers hardness of a ceramic is measured by indenting a pyramid-shaped tip (**Figure 10**) and then measuring the diagonal dimensions of the indent to determine the contact area [43].

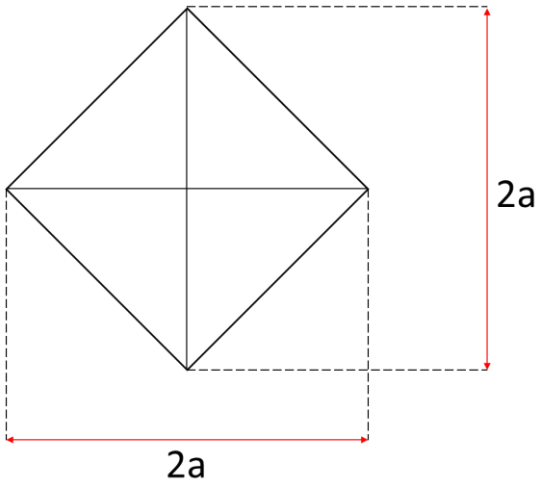

Figure 10. Schematic diagram of Vickers indent. Contact area showed in "a" dimensions.

However, the indenter shape changes when a Knoop indenter is used, due to a higher length to width indenter size ratio of 7:1, which disperse the load over a larger area. The purpose of using Knoop indenter is not only to change the indentation zone, but also to reduce the amount of cracking produced when the Vickers indenter is used [85]. The Knoop hardness of a ceramic measures only the length of the long axis and the projected area is calculated rather than the contact area. These values are greatly dependent on several parameters associated with the measuring technique, such as the indentation load, dwell time, sample

preparation and testing environment [48]. The indentation size effect (ISE) is described as the change of mechanical properties determined by indentation. It was shown that the decrease of the indent size leads to both increasing hardness and reducing plasticity, determined by indentation [86]. When a large load is applied, the hardness values show a plateau, so in order to make an accurate measurement, different loads must be used. To characterize the hardness of a ceramic material, it is important to comprehend ISE, since measured hardness is a value of the limit of a non-recoverable deformation of a ceramic [87]. The accuracy of this method will depend on the smoothness of the surface. Additionally, the thickness of the sample needs to be at least 10 times higher than the indentation depth. Cracking of the surface around the Vickers impression may alter the shape and clarity of the indentation, which could lead to an inaccurate measurement [88]. External and internal porosity can interfere with the measurements, especially if the tip falls directly in a large pore. The porosity of ceramics is correlated with the mechanical properties, therefore reducing the percentage of defects in ceramic is a common way to increase the hardness [45].

Even though errors in the measurements can be caused by the physical morphology of the sample and preparation, the biggest source of error comes from the uncertainties with the measurements of the diagonal length, as well as the equipment calibration, inadequate magnification power, human error, and poor image quality [89].

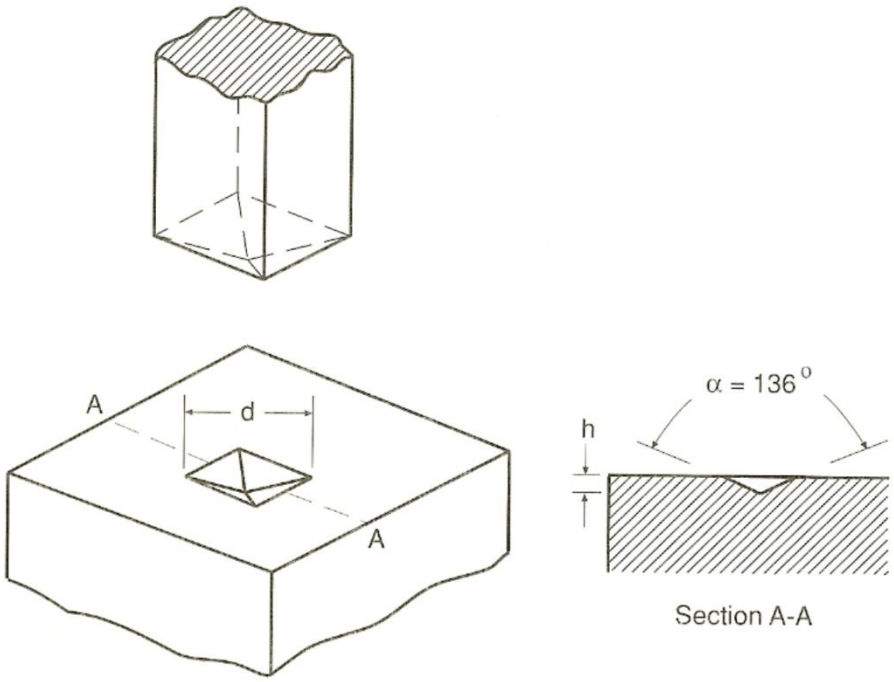

Figure 11. Vickers microhardness indentation technique [54].

1.6.2. Strength

The strength is defined as the ability to withstand an applied load without suffering a failure of plastic deformation [90]. The flexure strength of a ceramic material (σ_{fb}) is a degree of the ultimate strength of continuous fiber-reinforced ceramic composites in the form of rectangular bars formed directly or cut from sheets, plates or molded shapes undergoing bending. Another definition is the maximum surface stress existing in a bent beam at the moment of failure [91]. Other common names for flexure strength are bend strength or modulus of rupture; it is measured in terms of stress units (MPa, psi). A determined load applied to a material will produce internal forces known as stress. These forces cause deformation commonly called strain. The strength measures the stress required to break bonds, ultimate stress the material can handle without suffering fracture.

Flexure tests offer information on the strength and deformation of materials under complex flexural stress circumstances. The flexure strength is controlled by some specific parameters related to the testing procedure, such as environment, strain rate, specimen size, sample preparation, and fixtures. Additionally, time-dependent properties, such as slow crack growth and stress corrosion that can interfere with the measurements at room or elevated temperatures play a significant role [92]. Flexure strength is directly dependent on the sample resistance to fracture, size and number of flaws. It is worth mentioning that nonlinear stress-strain behavior may develop as the result of cumulative damage process (i.e. matrix cracking, matrix/fiber debonding, fiber fracture, delamination, etc.), variations on these parameters can produce errors or lack of consistency in the results for a given test specimen [51]. Due to a great importance of a porosity for the mechanical properties of ceramic materials, reducing the number of defects is fundamental way to increase the flexure strength. The flexure strength values do not fluctuate greatly, but they may vary slightly from one measurement or sample to another, in consequence, is important to consider the experimental errors.

At high temperatures, the creep phenomena behavior changes causing stress relaxation during the test; the flexure values of a ceramic can change depending on the machining techniques, materials' density, grain size, flaws or cracks. The sample preparation can produce surface machining damage; which can be random interfering or inherent part of the strength characteristics, , of which either, can lead to slow crack growth, residual stress provoking a rate dependency of flexural strength.

The flexure strength can be measured using either three points or four-point bending test; these methods eliminate the gripping problem associated with the specimen. The strength

is calculated by measuring the load needed the material to failure; it is calculated according to the equation 2. Where M is the bending moment, Y distance from the neutral axis and I is the moment of inertia.

$$\sigma = \frac{M_y}{I} \tag{2}$$

Four-point bending test is preferred because the gage section of the sample exposed to the highest bending moment, as opposed to the three-point configuration, which tends to overestimate the flexure strength value due to stress concentration accumulated at this point. **Figure 12** demonstrates shear and bending moment diagrams of three and four-point bending tests.

Shear is presented across the entire bar with an inconsistent moment during the 3-points bending test. The shear force is neutralized with a bending moment constant across the top loading pins for 4-point bending configuration, therefore 4-point bending test provides more accurate measurements with less influence of shear forces. [45].

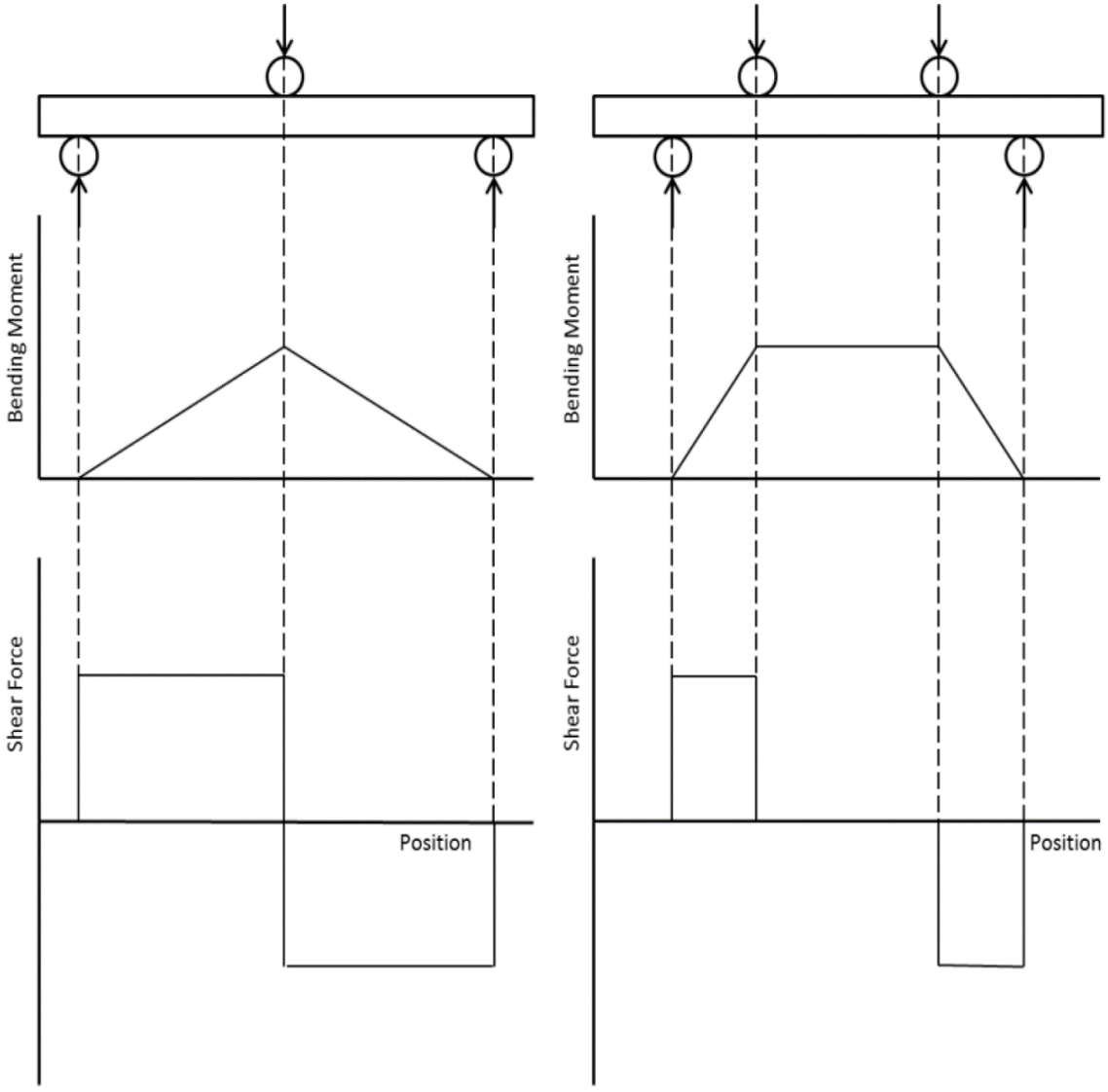

Figure 12. Shear and momentum diagrams for Three point (left) and four-point (right) bending.

2. Experimental Procedure

2.1. Raw material specifications

The raw materials used for this research were obtained by General Atomics Corporation, located in San Diego, California. The powder used was β-SiC, 45-65 nm size (US Research Nanomaterials, Inc, US2028, CAS#409-21-2). The powder was free of metallic impurities or sintering additives. There were no time-consuming processing steps like mixing, milling, or any other green processing; making this material ideal for the current research. **Figure 13** shows a micrograph of the as received SiC powder.

According to manufacturers' data, the manufacturing method was plasma chemical vapor deposition (CVD), with a specific surface area of 40-80 m^2/g, true density of 3.216g/cm^3, and particle size of 45-65nm.

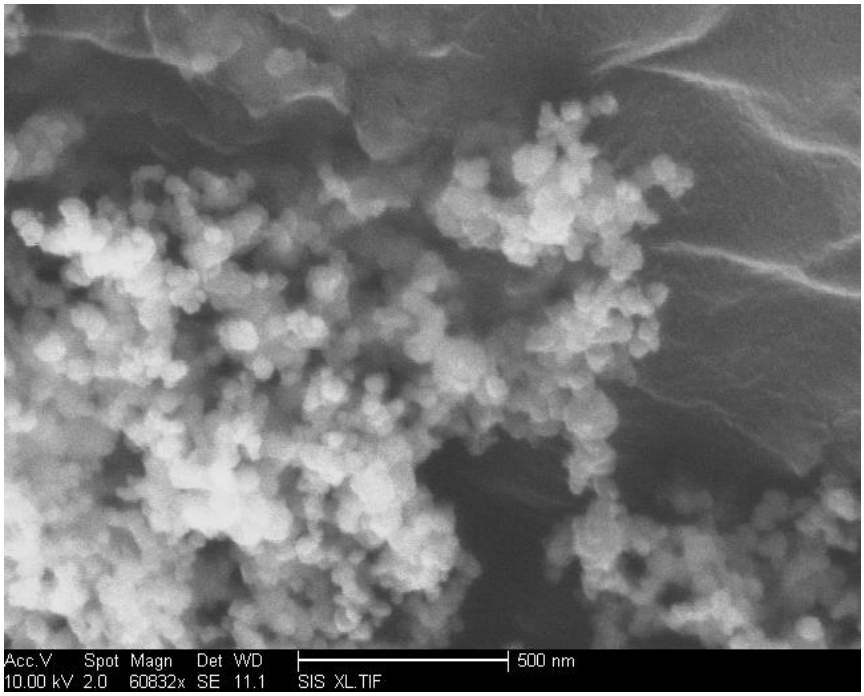

Figure 13. SEM image of as-received β-SiC nanopowder (US2028).

The SiC fibers used were Tyranno SA (Grade III) (UBE Industries, Ltd., Yamaguchi, Japan). Tyranno Fiber SA is a polycrystalline SiC fiber with a small volume of Aluminum, produced by decomposing and sintering of the amorphous Si-Al-C-O fiber. It possess high tensile strength, great elastic modulus, exhibits no strength degradation or compositional variations under heating up to 1900°C in an inert atmosphere (or in air up to 1000°C). The great advantage of this material is its crystallinity and near-stoichiometric SiC composition. In addition, the absence of oxygen and perfect crystallization makes it a perfect candidate for fabricating SiC/SiC composites at relatively high temperature and under harsh conditions, such as SPS.

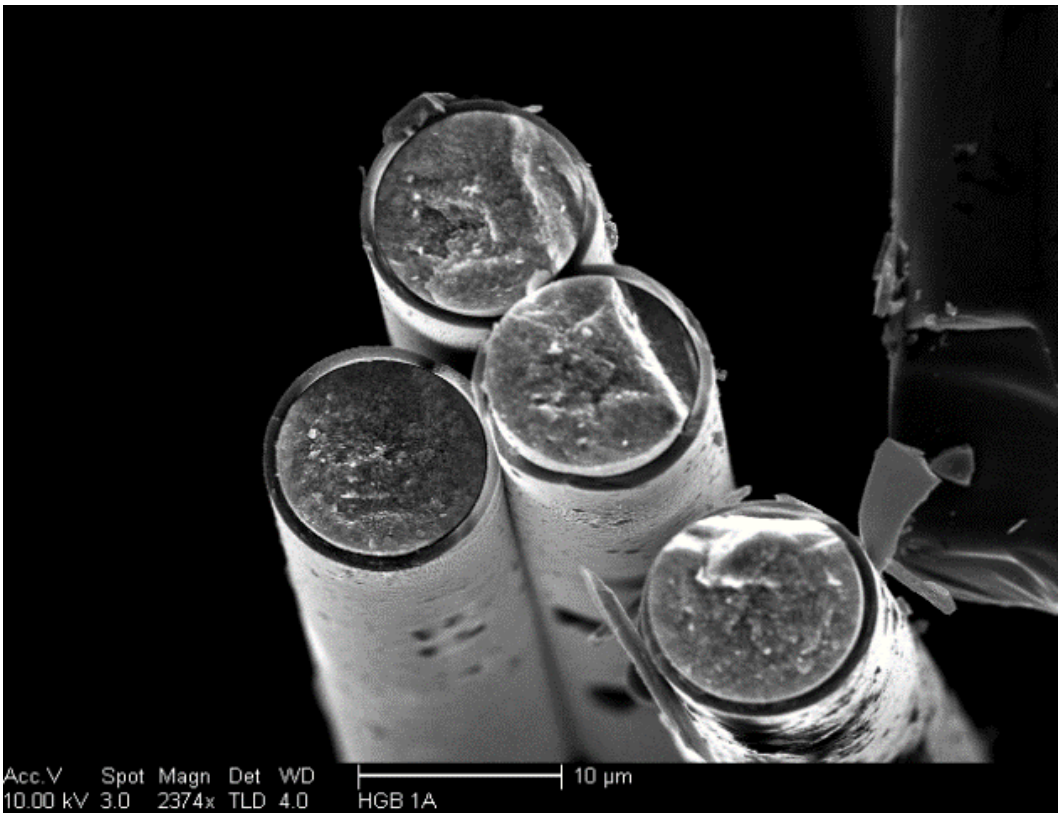

Figure 14. SiC fiber with PyC coating.

The SiC fibers were coated by pyrolytic carbon (PyC), using CVD with a methane precursor. The thickness of the fiber coating was 450nm. **Figure 14** shows an SEM image of the Tyranno-SA SiC fiber coated with PyC, the image demonstrated a good adhesion between the fibers and coating layers. PyC-coated Tyranno SA fiber tows were used as reinforcement for SiC/SiC composite fabrication in the current study. Typical properties of the newly produced (Grade III) Tyranno SA fiber are listed in Table 2.

Table 2. Properties of Tyranno SA Fibers (Grade III) [93].

SiC fiber	C/Si atomic ratio	Diameter (μm)	Density (g/cm3)	Filaments/yarn	Tensile Strength (Gpa)	Elastic Modulus (Gpa)
Tyranno SA	1.08	7.5	3.1	1600	~2.5	~410

The graphite dies, used for the sintering process of this project were machined with our specific design by Electrodes Inc. (Milford, Connecticut). On **Figure 15** the graphite die with both plungers is shown along with all the size specifications. The manufacturing material was high purity, high-density graphite 1-85. This kind of material is engineered to achieve maximum performance: wear resistance, surface finish and machining detail are commonly used for electronic, medical and aerospace applications. The graphite dies were 19mm in diameter; the plunger diameter is 0.25 mm less than the diameter of the die (the graphite paper sleeve, of thickness =1.5 mm, will be used to line the die). According to manufacturers' data, the dies present an apparent density of 1.85 g/cm^3, electrical resistivity 0.00052 Ohm/in, flexural strength 13,600 psi, particle size <4μm and 6.21 GPa hardness.

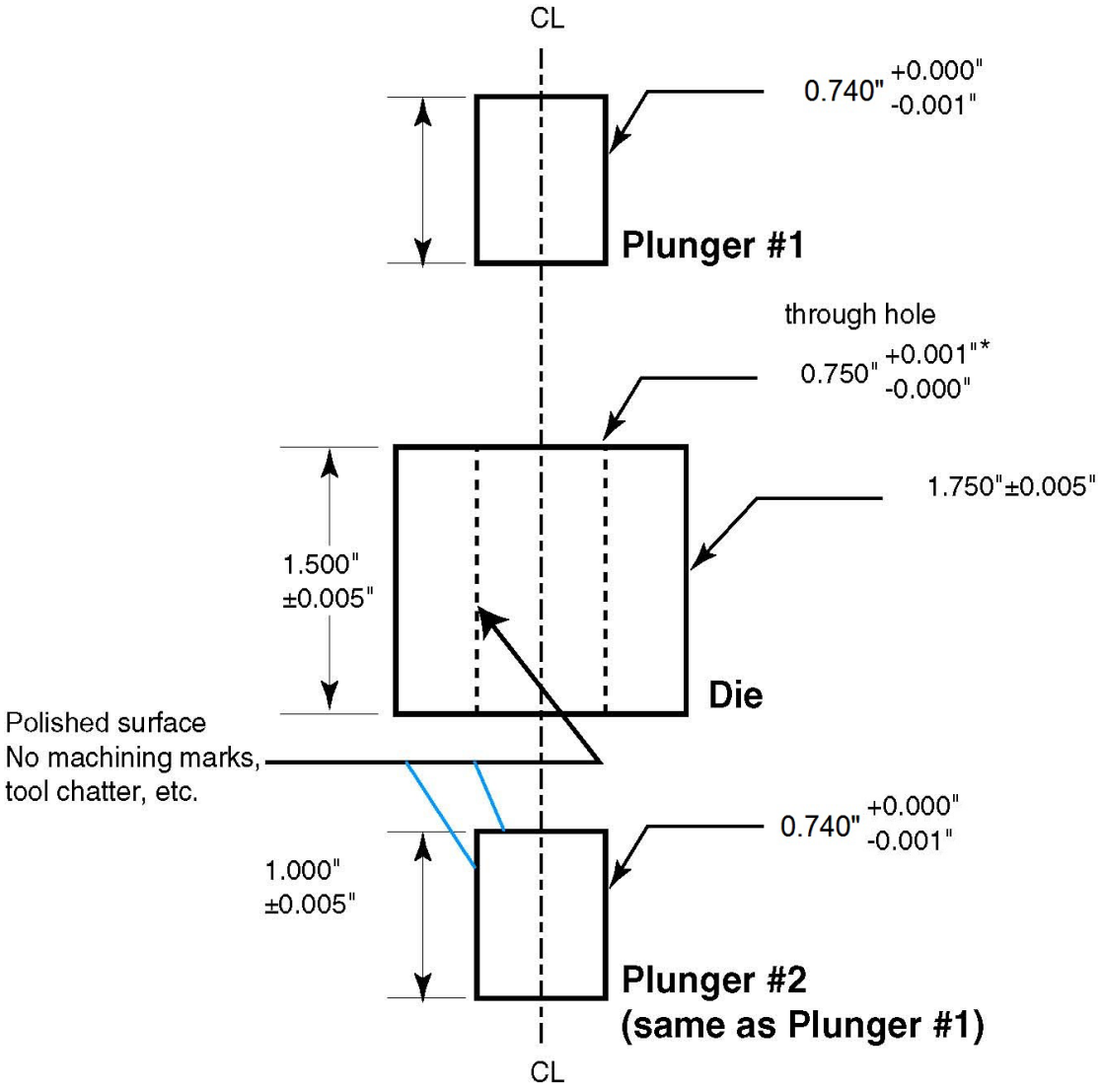

Figure 15. Graphite die measurement design.

2.2. Material characterization techniques

2.2.1. Electronic Microscopy

Materials were characterized for particle size and shape by field emission environmental scanning electron microscope (FEI/Phillips, XL30 ESEM, Hillsboro, OR) providing high resolution (500nm at 20kV) secondary electron images for surface morphology. Additionally, the solid state Back Scattered Electron Detector can be used to

accentuate atomic number contrast. Operating the ESEM in environmental mode (low vacuum) allows the user to image non-conducting samples without metal coating. The system also has an Oxford EDX system installed for energy dispersive X-ray microanalysis.

In addition, FEI Tecnai G2 Sphera 200KV transmission electron microscopy (TEM) (FEI Company, Hillsboro, OR) and Ultra High-Resolution scanning electron microscope (FEI SFEG UHR SEM, Hillsboro, OR) featuring the FEI Sirion column, which enables high-resolution secondary electron imaging at low kV. Using UHR mode and the Through Lens Detector, resolution of 1nm is possible at 10kV or higher and 1.7nm at 1kV. An EDX SDD (Silicon Drift Detector) system by iXRF is also installed on the UHR SEM for energy dispersive X-ray microanalysis.

2.2.2. X-Ray Diffraction

The powder composition and crystallographic orientation were determined using a BRUKER D2 Phase X-ray diffractometer (XRD), with Cu Kα source. The XRD technique involves directing an incident X-ray beam at the sample. Upon hitting the sample, the X-rays are elastically scattered due to the long-range order of the crystal structure within the sample. The intensity of the scattered X-rays is detected and plotted for a range of angles (2θ). The resulting intensity charted over ranging angles acts as a fingerprint for the material. These charts are then compared to an extensive database to determine the composition and crystallographic orientation.

2.2.3. Hardness

The sample's hardness was evaluated using an LECO LM810AT with a Vicker's hardness indenter. The Vicker's hardness of a ceramics is measured by an indentation of a

material with a pyramid-shaped tip (see **Figure 4)** with the subsequent measuring of the diagonal lengths using an optical microscope. The hardness measures the resistance from a material to a non-recoverable plastic deformation and can be affected by the density of the material and imperfections on its surface.

2.2.4. Flexure Stress

The flexure properties of the SiC composite samples were measured using an Instron electromechanical universal testing machine (model 2519-104) with a 500 N load cell capacity, from bending tests. The Instron system can be configured with a variety of grips, flex fixtures, and extensometers to meet the ASTM C1341-13 standard requirements. The results obtained were corresponding stress and strain. Stress is the load over a material's area that will produce known internal forces that can cause fracture due to bending. The strain is the plastic or elastic deformation caused by the stress.

2.3. Sample Assembly

2.3.1. No Reinforcement Samples

Before sintering, β-SiC US2022 powder provided by General Atomics Corporation was used to produce non-reinforcement samples. A 2.0 gram target powder mass was used for all the samples. A 40x60 mm graphite foil was cut and lined to the die inner hole, to cover the surface that would connect die and sample. For consistency, the die was weighed, the powder was added directly to the die, while consequently the mass measurement was taken. After the powders were weighed and recorded, the die assembly was closed and ready for sintering.

2.3.2. Fiber Reinforced Samples

Before sintering, the material used for this assembly was β-SiC US2022 powder and 9 mm radius Tyranno SA (Grade III) fiber plies provided by General Atomics Corporation. A 1.0 gram target powder mass was used for all the samples. A 40x60 mm graphite foil was cut and introduced on the die hole, to cover the surface that will be in contact with the die and sample. To maintain consistency, the die was weighed, the distribution of the material was made depending on the fiber volume fraction (FVF) laminates, which is calculated by:

$$V_f = \frac{m_f \rho_m}{m_f \rho_m + \rho_f (m_c - m_f)} * 100\% \quad (9)$$

$\rho_f =$ Volume density of the SiC fiber
$\rho_m =$ Density of the SiC matrix
$m_c =$ Total mass of the sample
$m_f =$ Fiber mass

Using the following order:

- **31.5 %:** 0.33g→ 1st plie→ 0.33g→ 2nd Plie→ 0.33g
- **40.8 %:** 0.25g→ 1st plie→ 0.25g→ 2nd Plie→ 0.25g→ 3rd Plie→ 0.25g
- **47.9 %:** 0.20g→ 1st plie→ 0.20g→ 2nd Plie→ 0.20g→ 3rd Plie→ 0.20g→ 4th Plie→ 0.20g

The powder was added directly to the die, while consequently the mass measurement was taken. After the powders were weighed and recorded, the die assembly was closed and ready for sintering.

2.4. Spark Plasma Sintering

Samples were sintered in an SPS system, model HD D10 made by FCT Systeme GmbH. This system can fit samples up to 80mm in diameter. The equipment can apply a maximum force of 200MPa, with a maximum heating rate of 300ºC/min. The system is operated by a touchscreen interface using the ECS 2000 software package by Stange Elektronik GmbH.

The highest and lowest temperatures were defined based on the minimum temperature SiC can be sintered to a relative density greater than 90%, as well as the highest temperature the fibers could stand without suffering damage. Based on previous experience using SiC on this equipment, as well as a literature review, the samples were sintered on the temperature range 1550°C - 1750°C under a uniaxial pressure of 100MPa. The heating rate used for all the samples was 100°C/min.

The most critical monitored process parameter during the sintering was the temperature measured by pyrometer or thermocouples. The force applied translated into pressure across the sample, displacement or die's piston movement, and time. Other process parameters were monitored, but will not be discussed in this work.

After the sample assembly was finished, the die was placed inside the SPS system chamber, between the hydraulic pistons. The graphite die was pressed by the upper and lower piston. At the same time, a high density current is passed from the upper steel piston, through the graphite die, the composite and then to the lower piston. The current resistively increases the temperature of the graphite and the composite, while pressure is applied causing the composite to densify. During the sintering process, the heat in the pistons is monitored using

thermocouples; the sample temperature is registered by the pyrometer. To prevent heat loss or temperature gradient on the sample, the graphite die assembly is wrapped with a carbon wool material (heat jacket). Once the previous steps were done, the chamber is evacuated to a pressure of 10^{-3} Torr. The program starts after the ideal pressure is reached; all samples manufactured for the current research were sintered under vacuum with no additional gases. All samples were made following a similar systematic method to reduce any variability.

2.5. Flexural strength

Three-point bend testing was performed on the sintered materials, to find an improvement in fracture resistivity during loading. The flexural strength test parameters were adapted from ASTM C1341-13 standard for continuous fiber reinforced advanced ceramic composites (CFRCC) [94]. Specimens were cut in the form of rectangular bars 20mm by 4mm with their thickness ~1mm. A three-point loading system was employed, with two-fixture support bars of 5mm in diameter; the force was applied using a loading roller bar between the supports. A picture of the three-point bend test fixtures and equipment used is shown in **Figure 16**. Generally, this test method is used for material development, quality control, and material flexural specific conditions.

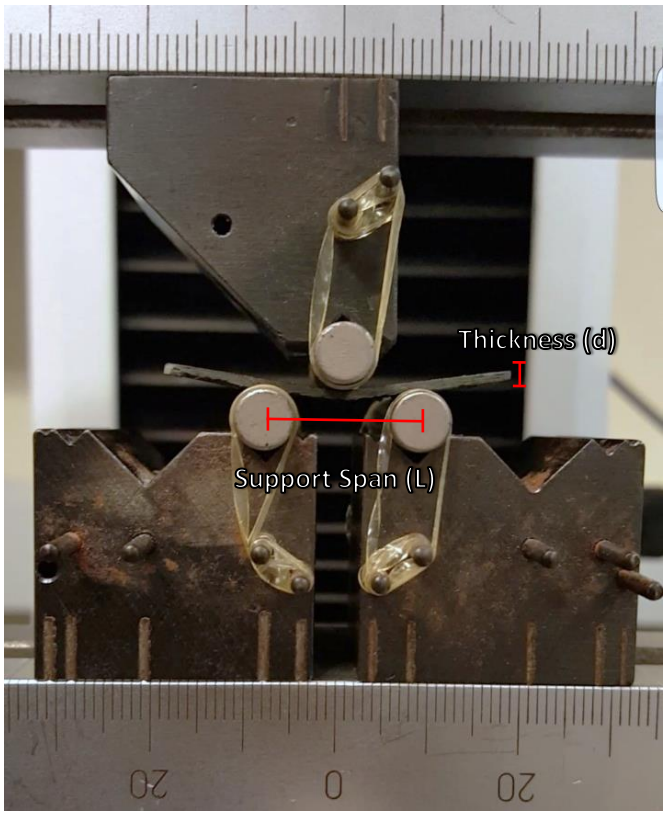

Figure 16. A picture of the 3-point bending test fixtures showing a visible sample bending.

Flexure tests offer data on the strength and deformation of materials under complex flexural stress conditions. In fiber reinforced advanced ceramic composites the strain-stress behavior may be caused as a consequence of multiple factors as matrix cracking matrix cracking, matrix/fiber debonding, fiber fracture or delamination [57]. However, to obtain a valid flexural strength value, the material must fail in the outer fiber surface in compression or tension, rather than by shear failure.

This is done by maintaining a high ratio between the support span (L) and the thickness/depth (d) of the test specimen, as presented in table 3. This L/d ratio is kept at values of ≥16 for 3-point testing. If the span-to-depth ratio is too low, the test specimen may fail in shear, invalidating the test.

To keep the correct dimension, for samples with a width higher than 3mm, the width must not exceed one-fourth of the support span. The length of the specimen should be long enough to allow an overhanging in the outer support of at least 5% of the support span but in no case less than 5 mm on each end [52].

Table 3. Recommended dimensions for three-point bending test at 16 to 1 support span to depth ratio.

Nominal test specimen Depth/ Thickness (mm)	test specimen Width (mm)	test specimen Length (mm)	Support Span (mm)	Rate of Cross-Head[A] Motion (mm/s)
L/d = 16 to 1				
1	3	26	16	0.04
2	6	45	32	0.09
3	9	60	48	0.13
4	12	75	64	0.17
5	15	90	80	0.21
6	18	105	96	0.26
10	30	180	160	0.43
15	45	270	240	0.64
20	60	360	320	0.86

To identify the possible strengthening mechanism under a precise fracture of the CFCC, displacement or strain control are the preferred option. However, if a rapid test rate needs to be used, there may be differences in the fracture process, and these test control modes may be inappropriate.

Strain rate: Is a method of controlling tests of deformation processes to avoid runaway conditions, which is an independent variable in a nonlinear mechanism as yielding. Strain rate can be related to the stress rate by the following equation:

$$\varepsilon' = \frac{d\varepsilon}{dt} = \frac{\sigma}{E} \tag{3}$$

t = Time (s)
ε’ = Strain rate (s^{-1})
E = Elastic modulus (MPa)
σ = Maximum stress rate (MPa)
ε = Maximum strain on the outer fibers

For this kind of material, the recommended strain rate is on the order of (1-10) $x10^{-3}s^{-1}$ to minimize environmentally and force application rate effects.

Displacement rate: Is the control of the test machine crosshead to mechanically apply force to the test specimen. Depending on the geometry, cross head displacement is calculated as follows:

$$D = \frac{0.167\varepsilon L^2}{d} \tag{4}$$

L = Outer support span (mm)
d = test specimen thickness (mm)
ε = desired strain rate (mm/mm*s)
D = Rate of cross head motion (mm/min)
1000 $x10^{-6}$ s^{-1} strain rate is recommended for initial testing.

Flexure stress: The stress experimented by the sample beam when achieving the maximum tensile, compressive stress, during the flexure test.

$$\sigma = \frac{3PL}{2bd^2} \tag{5}$$

L = Outer support span (mm)
b = Test specimen width (mm)
d = Test specimen thickness (mm)
P = Force at given point in the test (N)
σ = Maximum stress at a given force (MPa)

Flexure strain: The displacement or deflection produced at a test specimen during flexure stress.

$$\varepsilon = \frac{6Dd}{L^2} \tag{6}$$

L = Outer support span (mm)
d = Test specimen thickness (mm)
D = Deflection at beam center (mm)
ε = Maximum strain in the outer fibers (mm/mm)

A schematic representation of the stress-strain behavior of an unreinforced matrix and a CFCC is presented in **Figure 17**.

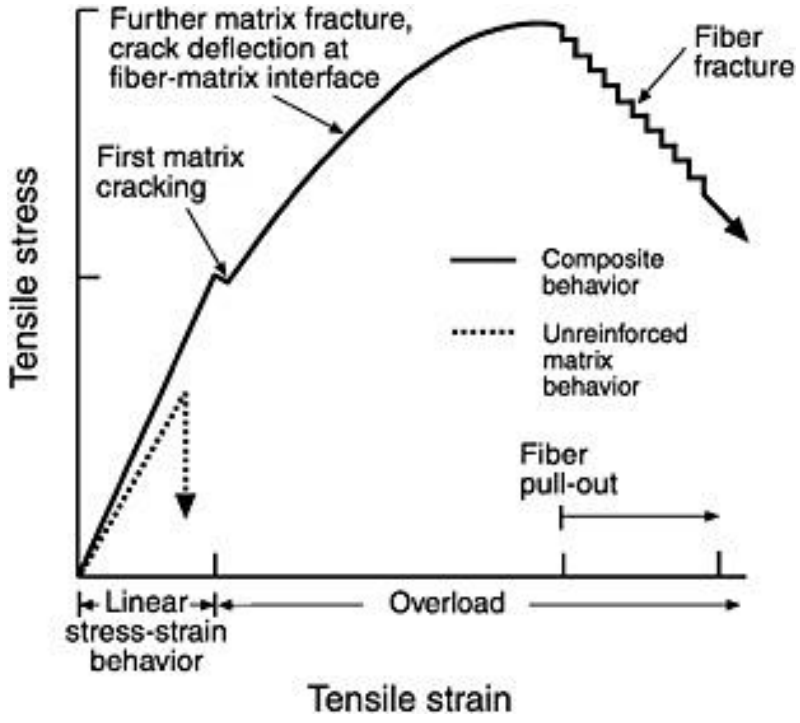

Figure 17. Load-displacement stress-strain curve of CFCC's [95] .

2.6. Microhardness

The microhardness testing method used for the SiC specimens covers the determinations of the Vicker's indentation hardness of advanced ceramics. The method can be summarized as an indentation hardness test used in a calibrated machine to force a pointed, square base, with pyramidal diamond indenter having specified angles, under a predetermined load, into the surface of the SiC tested material, to measure the diagonals projected on the surface of the resulting impressions after the load removal, which are measured using an optical microscope.

Microhardness measurements were made using an LECO LM810AT hardness tester unit. A picture of the microhardness testing unit can be found in **Figure 18**. The hardness tests were done using a Vicker's hardness indenter, which was previously calibrated using a known constant. The specimen was cleaned and free of any grease or film, was placed on the stage of the equipment to secure the sample from rocking or shifting during the measurement.

A mass of 500 ground force (GF) and a hold time of 10 seconds were used during the testing of all sintered samples. Five iterations were made across the thickness of the sample, to reduce error and variation that may occur in the radial direction, with a similar distance between each measured point. This method was used to achieve consistent comparative data and reduce errors or any variability in the measurements.

Vicker's indentations results may be influenced by different factors as surface flatness, parallelism and surface finish. The Vicker's indenter is likely to cause cracks in advance ceramics due to its brittle nature, and the cracks may influence the measured hardness by basically changing the deformation process that contributes to the formation of an impression, impairing or precluding the measurement of the diagonal length due to caused damage to the indentation tip or side [52].

Cracking or spalling around Vicker's impression can happen and change the shape and clarity, especially for the coarse-grained samples, where the grains can cleave and dislodge. Porosity on or below the surface can also affect the measurements, especially if the indentation falls directly onto a large pore.

Figure 18. Picture of LECO LM810AT microhardness testing unit.

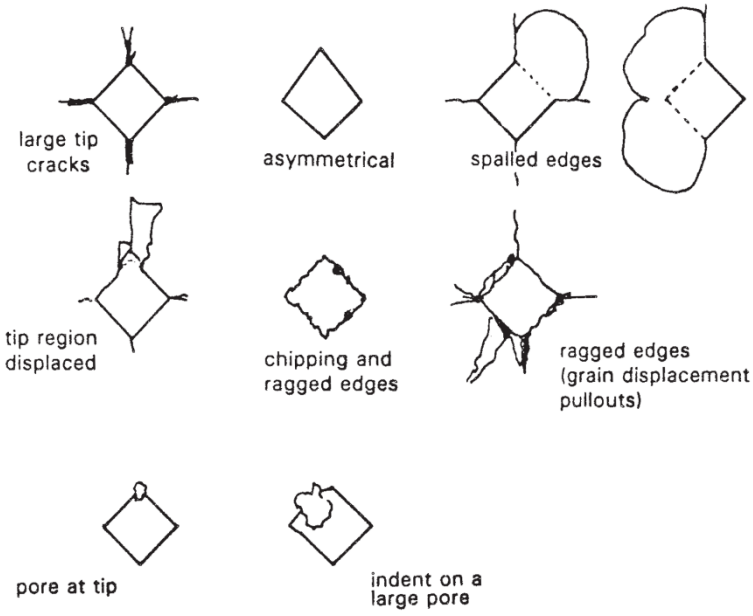

Figure 19. Guidelines for the unacceptable indentations.

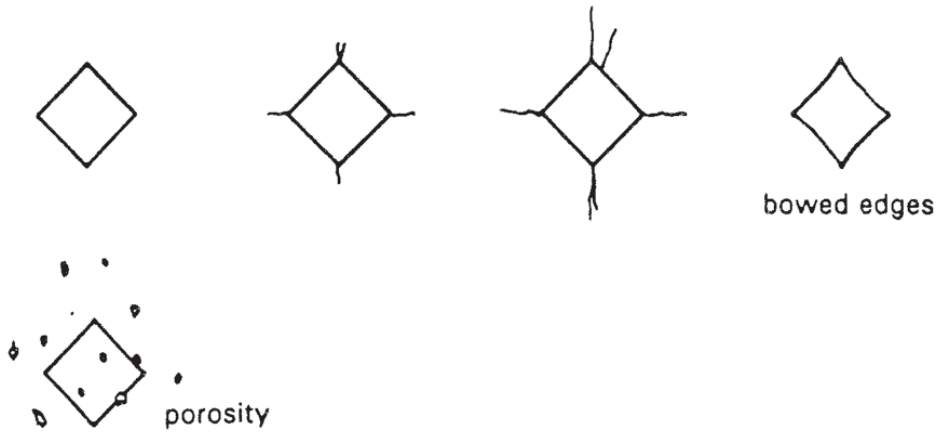

Figure 20. Guidelines for the acceptable indentations.

A representation of the unacceptable indentation methods is presented on **Figure 19**. If there is an excessive cracking from the indentation tips and sides, asymmetric marks, large pore or any other presented on the figure, the indentation shall be discarded from measurement. The acceptable ways to make an indentation are shown on **Figure 20**. It is important to remember that for advanced ceramics, at least five acceptable indentations should be made to achieve consistent comparative data.

A diamond indenter, with a pyramidal shape, a quadrangular base and an obtuse angle of 136° between opposite faces, is hard pressed into the material under a load F. Vicker's Hardness may be calculated and reported regarding either GPa units or Vicker's hardness number and is calculated using the following equation:

$$H_v = 0.1889 \frac{F}{L^2} \tag{7}$$

Where L=(X+Y)/2, L is the diagonal is square impressions (mm), X is the horizontal length (mm), Y is the vertical length (mm), and F is the applied load (N).

2.7. Sample Preparation

After the sintering, the samples were removed from the graphite die by hand or using a hydraulic press. The graphite foil was peeled from the surface of the sample and cleaned with a wire brush. The samples were then polished using a coarse grit to remove the rest of the foil. Next, the samples were rinsed, cleaned and fried to remove any contaminant present polishing. The finishing step was to characterize the composite to determine specific properties like density, microhardness, microstructure and flexural strength.

The density measurements were made on the Mettler Toledo (MS104S/03) apparatus, the calculations were assessed by the Archimedes method as appears in equation 1, and were measured before cutting any of the disks. To calculate the density the sample disks were dried in the furnace at ~120°C for 24 hours, followed by recording the dry weight. Next, the samples were submerged in deionized water, suspended from metal mesh to secure samples and prevent cracking and keep it under vacuum for 1 hour. The samples were again weighed while submerged in deionized water to measure the suspended weight. Finally, the saturated samples were removed from the water, brushed with a damp cloth to remove surface water, and recorded the saturated weight. The process was performed five times for each sample to confirm the results

$$Density\ of\ sample = \frac{Weight\ of\ sample * Density\ of\ water}{Weight\ of\ sample - Weight\ of\ sample\ in\ water} \quad (8)$$

After calculating the density, the sample was put through different preparation steps before bending tests, microhardness and microstructure. These steps involve cutting, mounting and polishing the samples. The samples were first cut using an electrical discharge machining

(EDM) precision cutting tool. A picture of the EDM equipment is presented on **Figure 22**.

The SPS and HP sintered samples were cut in the pattern presented on **Figure 21.**

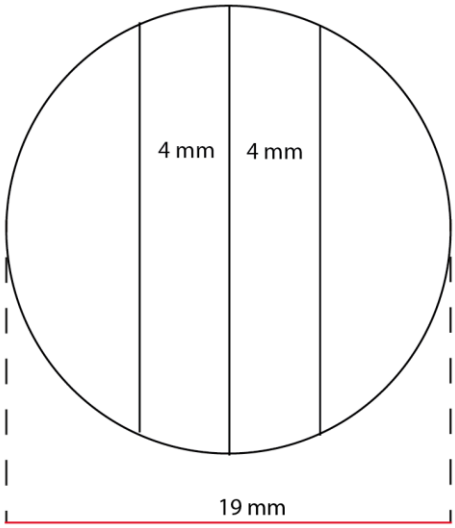

Figure 21. Schematic of the cutting pattern for SiC samples .

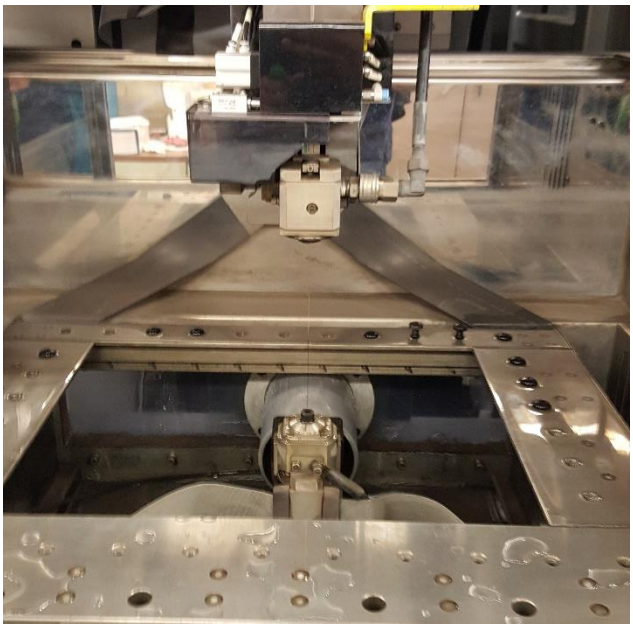

Figure 22. Picture of the electrical discharge machining equipment used to cut the SiC sample.

The surface preparation is an important requirement for a valid flexural stress, which is done by fine polishing to achieve a relatively smooth surface and remove imperfections. In addition, the test specimens must have a specific test specimen geometry provided by the ASTM standard to prevent shear fracture instead of bending. For this experiment due to the high hardness of the SiC sample disks, EDM was used to cut the sample taking advantage of its great accuracy.

After the bending test was performed, the sample became separated into two pieces due to the fracture caused by the bending. One of these pieces was selected for microhardness testing, while the second piece was used for fracture surface analysis.

For more accurate and reproducible results, microhardness testing needs to account for effects of sample size, preparation, and environment. The thickness of the specimen should be at least ten times as thick as the indentation depth, it should have a ground and polished surface, the roughness of the surface should be less than 0.1µm, since extremely rough surfaces may reduce the accuracy of indentation data, and the test must be performed at room temperature. To maintain these specifications, the samples were mounted on an epoxy mold to maintain stability and avoid movement during the test.

Once the samples were mounted, they were ground and polished on an Ted Pella. Inc XP 8 grinder and polisher tool. A picture can be found in **Figure 23**. The grinding and polishing followed specific and systematic steps listed in **Table 4**. After each step, the samples were cleaned using soap and isopropyl alcohol to remove media or residues from previous steps. The samples were also viewed under an optical microscope to confirm scratch removal after the process.

Figure 23. Picture of the grinding and polishing machine used to prepare the SiC samples.

	Grinding				Polishing		
Abrasive Type	Diamond	SiC	SiC	SiC	SiC	Diamond Suspension	Diamond Suspension
Size	2mm	400	600	800	1200	3µm	1µm
Lubricant type	water	water	water	water	water	D-Susp	D-Susp
Speed (RPM)	500	300	150	150	150	150	150
Time	5	5	3	3	3	1	1

Table 4. Grinding and polishing protocol used to prepare SiC samples.

3. Results and Discussion

3.1. Raw Material Characterization

Although specifications for the powder were provided by General Atomics Corporation and the vendor, the in-house characterization was performed to confirm their

data. To determine the size, shape, and distribution of the powder a field emission electron microscope technique was used. The secondary electron detector was selected to achieve higher resolution surface images. Even though backscattering detector yields to better compositional contrast, the secondary electron has a higher sensitive capability.

A small amount of SiC powder was placed on a two-sided carbon tape, the rest of the powder was removed using compressed air, mounted on the FE-SEM sample holder, and the samples were impregnated with Iridium to reduce the charging effects. All the samples were taken at the voltage operating range of 10-20kV, and a working distance of 10mm. The resolution of the images was clear and provided good topographical contrast.

The powder consists of an even distribution in both size and shape of the particles, as presented on **Figure 24** . This has a beneficial effect on the packing and green density [96]; the particles tend to be in agglomerates of 500 nm. A high level of particle agglomeration can produce densification problems [97], however the agglomerates in the sample appear to be on similar size order as the SiC particles. An estimation of the average approximate values has the particle size as less than 100 um.

Figure 25 shows a TEM micrography of the as-received SiC nanopowder at a much higher magnification. Thought by the examination of this image it can be determined that the size of the agglomerates is in the order of a few hundreds of nanometers and the particle sizes are 30-50nm, presenting a uniform size and shape distribution.

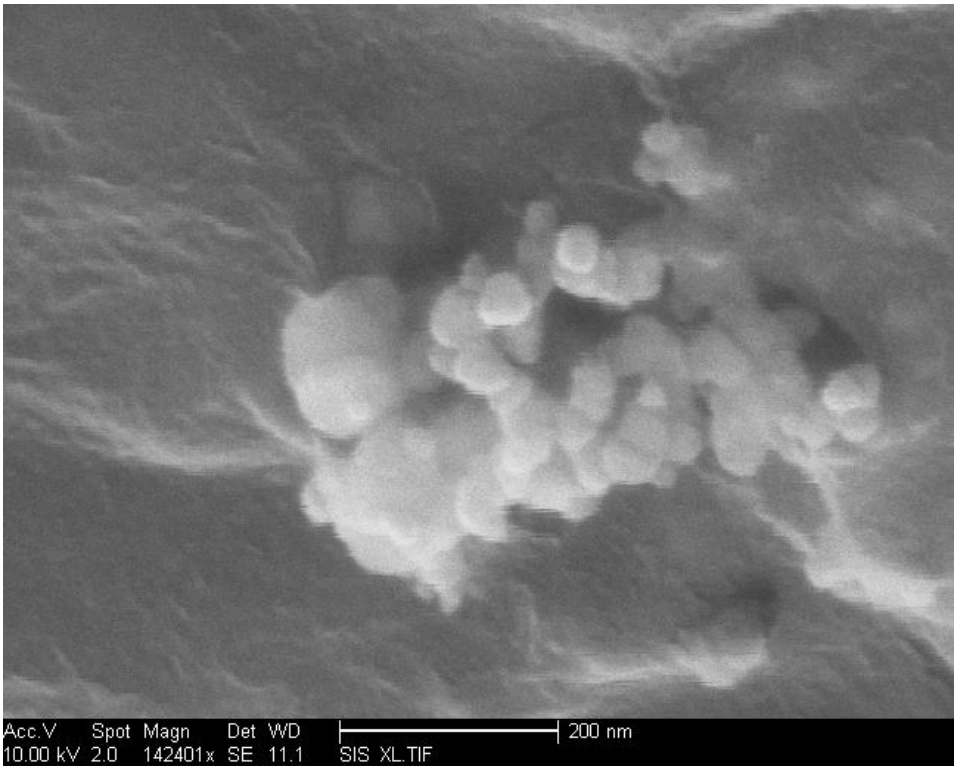

Figure 24. FE-SEM micrograph the as-received SiC nanopowder. The image shows agglomeration of approximately 500nm and powder sizes less than ~100nm.

The particle size (agglomerate size) distribution was determined using a light scattering technique. The process was executed at room temperature for 100 seconds. The nanopowder was dispersed in a 10 pH buffer solution. The intensity of the scattered light was detected and processed, to provide statistical information about the particle (agglomerate) size and range. The initial SiC nanopowder was also tested using X-Ray diffractometer to define the crystallographic composition and orientation. The X-ray diffraction (XRD) of the as-received raw material; the intensity of the diffractions was plotted as a function of the angle (2θ) as presented on **Figure 26** . It is clear that obtained spectrum corresponds to β-SiC.

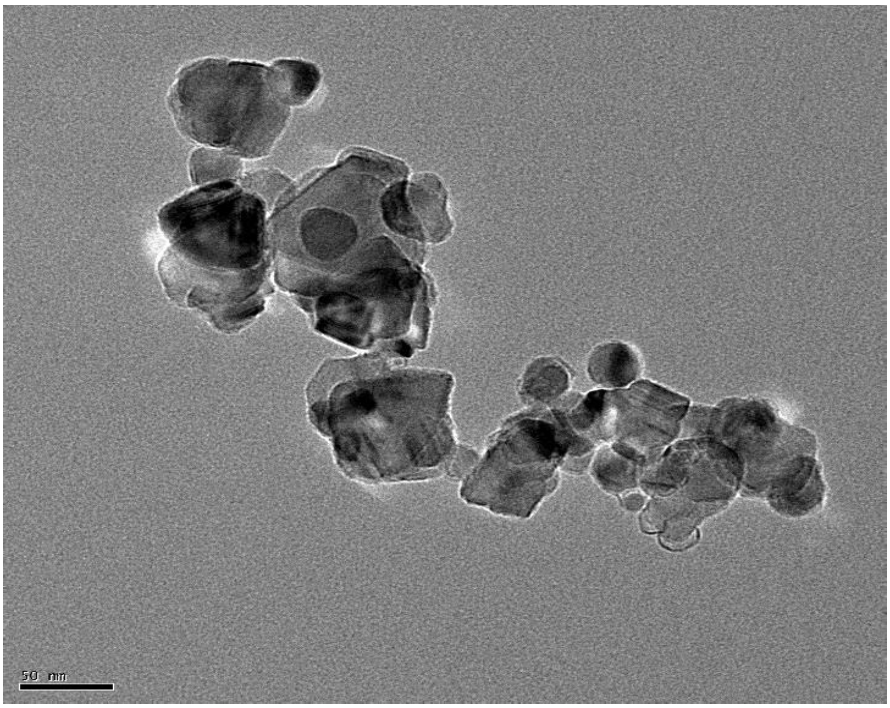

Figure 25. TEM Micrograph of the as-received SiC nanopowder. The image presents a particle size on the order of 30-50 nanometers.

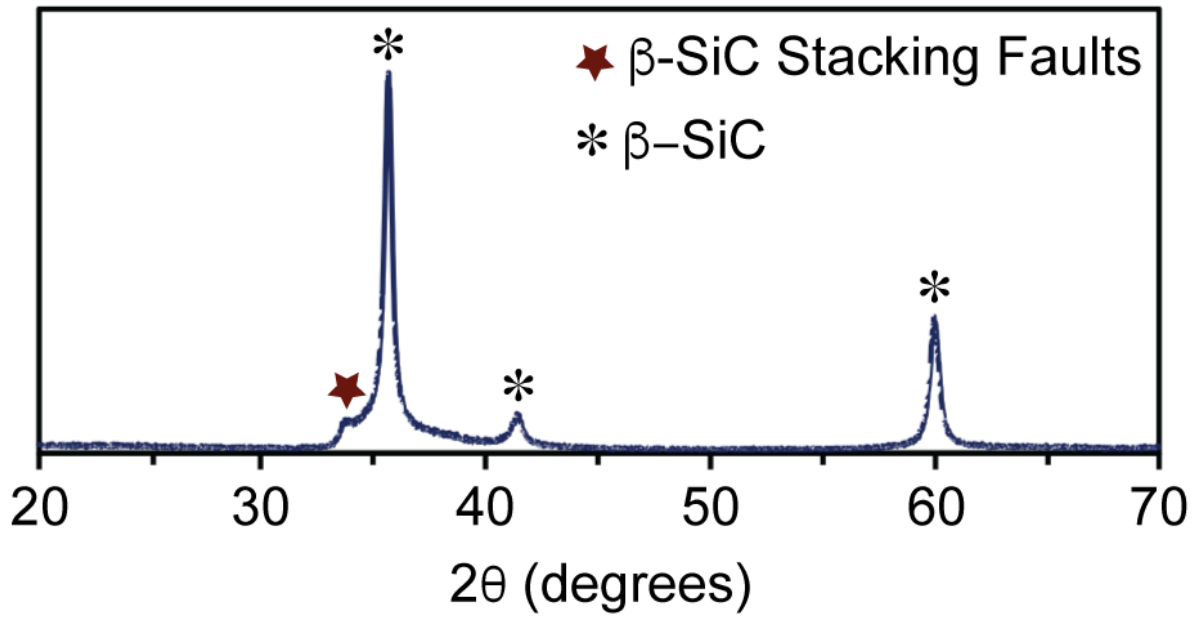

Figure 26. XRD results of the pristine SiC powder.

The experimentally obtained data present a correlation with the standard for SiC-3C. The peak locations are aligned correctly as well as the intensities of the predominant peaks. This demonstrates that the pristine material is composed mostly of SiC powder with the cubic crystallographic structure of the 3C polytype, also known as β-SiC. This polytype is formed at temperatures below 1700°C [Muranaka, 2008], with the benefit of a higher surface area compared to α form. The results indicate that the received powder mostly made of cubic structured β-SiC, with no additives present.

3.2. Monolithic SiC sintering

Using a wide temperature range, the objective is to find the ideal sintering temperature for the monolithic β-SiC. The powders were consolidated by Spark Plasma Sintering with no additives and no prior cold pressing. Table 5 shows the processing parameters for samples sintered at a different range of temperatures 1500°C – 1750°C, all of them under a pressure of 100 MPa and constant heating rate of 100°C/min. The final specimens were disks of 20 mm diameter and 2-3mm height.

Table 5. Sintering parameters used for step 1 samples.

Sample	Temperature (°C)	Pressure (MPa)	Heating Rate (°C/min)	Holding Time (min)	Density (g/cm^3)	Percentage (%)
1	1500	100	100	5	2.57	79.94 ±1.09
2	1550	100	100	5	2.98	92.81 ±0.98
3	1600	100	100	5	3.06	95.33 ±1.10
4	1650	100	100	5	3.11	96.88 ±0.85
5	1700	100	100	5	3.16	98.44 ±1.16
6	1750	100	100	5	3.10	96.57 ±0.89

Pure SiC Nanopowder (45-65 nm) - SPS

The density measurements on the sintered monolithic SiC material was determined by the well-known Archimedes' method. Table 5 shows the resulting density of samples sintered while varying the temperature at constant pressure. **Figure 27** shows relative density as a function of temperature for the sintered samples, it was determined by this plot that the density increased with temperature increment, the density from the sample sintered at 1500°C were significantly less than the sample sintered at 1700°C, by observing this chart it appears that the optimal sintering temperature lies somewhere between 1650°C and 1750°C exhibiting near theoretical density. This is better results than expected to present a relatively high density (98.44%) at a much lower temperature compared to the literature [98].

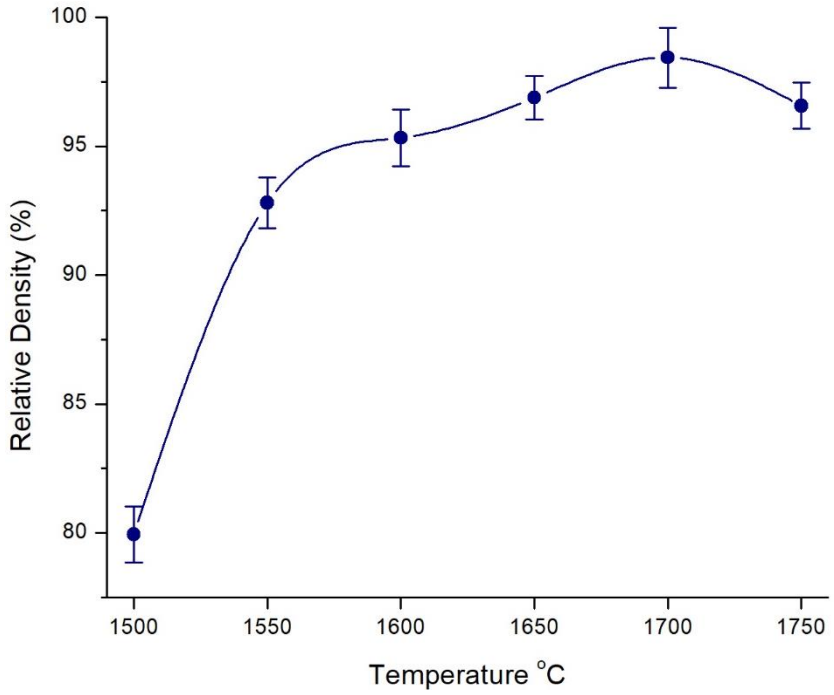

Figure 27. Density sintering parameters used for step 1 samples.

To confirm the porosity level on the samples, a microstructure examination was performed using a Field emission scanning electron microscopy, to observe porosity and shape of the particle, selected images were chosen to show comparative information. In

Figure 29 A) we can see a micrograph of sample 1 sintered at 1500°C, the micrograph shows a microstructure that does not seem to be fully dense. There is a substantial volume of porosity in the sample, and the grain structure does not appear to be fully developed, this microstructure appears to be consistent with the entire sample. In **Figure 29**. E) we can see a micrograph of sample 5 sintered at 1700°C, the micrograph shows a microstructure that appears to be fully dense, and correlates to Table 5, the sample with the highest relative density.

Upon comparing **Figure 29** A) and E) It was determined that a reduction in porosity and microstructure change, was directly related to the increase in temperature. The diffusion process is promoted at a higher temperature, enhancing the mass transport mechanisms, resulting in a homogeneous microstructure, density increase, and porosity reduction [99].

Figure 28 presents the X-Ray diffraction results for two of the sintered samples, the data for the most prominent peaks correlate well with the standard for 3C-SiC. This indicates that the sintered SiC samples are composed mostly by cubic structure SiC, except by the graphite fold signal, meaning that no phase transformation was developed during the process.

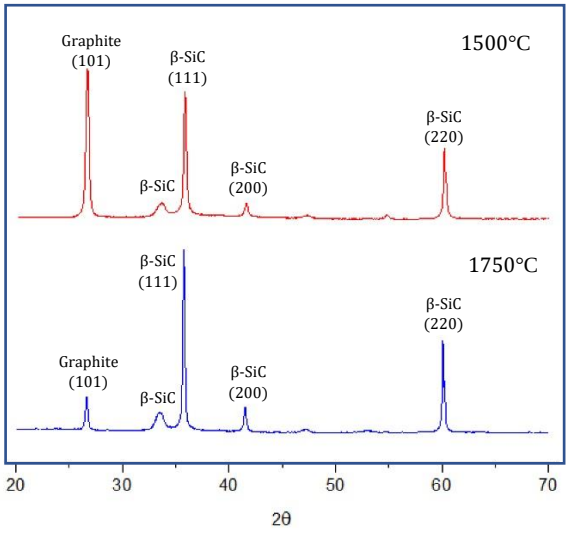

Figure 28. XRD Results of samples sintered at 1500°C and 1750°C.

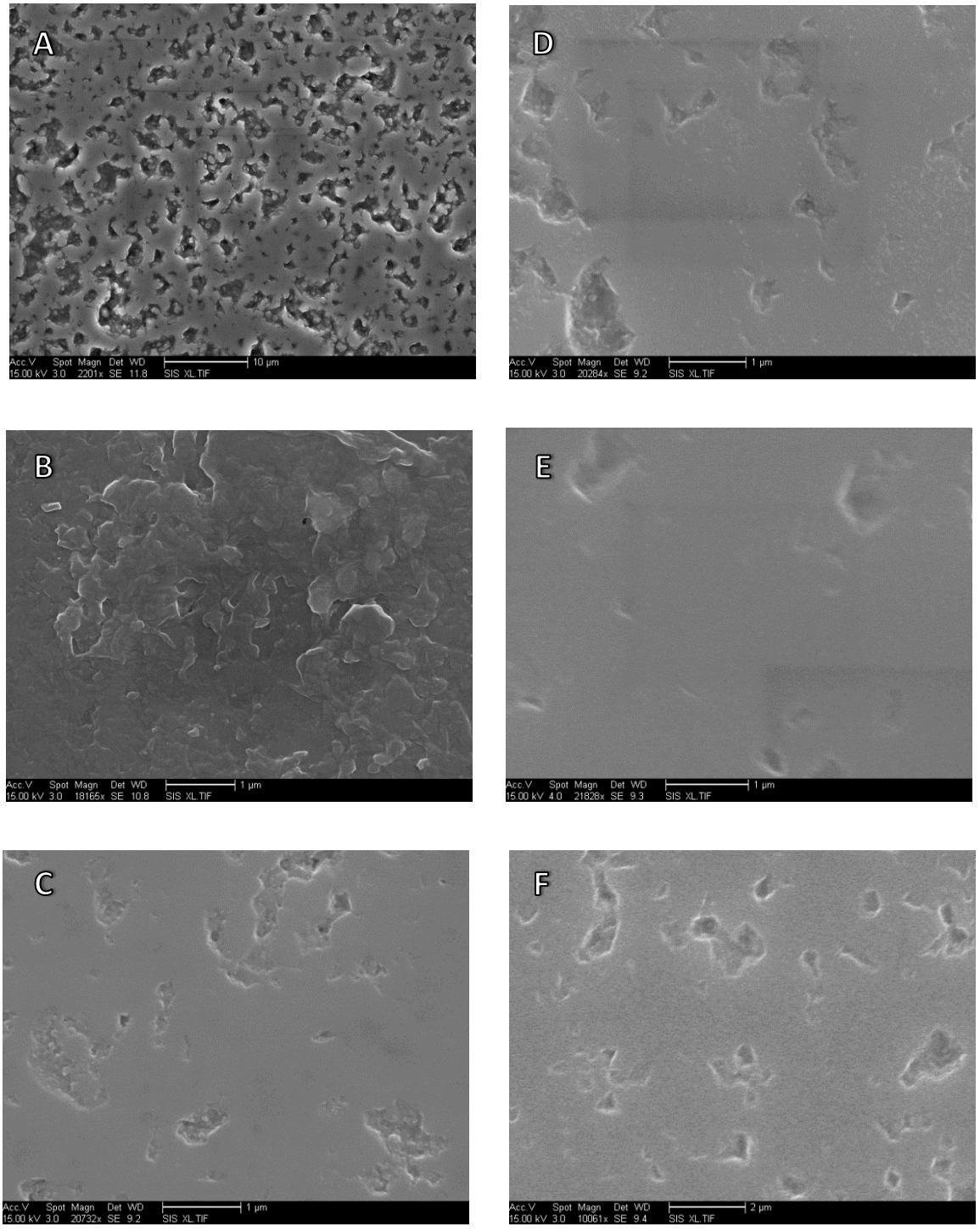

Figure 29. Step 1 – Polished Surface A) 1500ºC, B) 1550ºC, C) 1600ºC, D) 1650ºC, E) 1700ºC, F) 1750ºC.

3.3. SiC/SiC fiber reinforced composites processing

A comparison of the densification results of SiC/SiC composites sintered by SPS and HP was studied.

To define the best sintering temperature for the SiC powder in the presence of SiC Tyranno-SA fiber plies during the SPS consolidation, the experiments with higher density and best microstructure during the monolithic SiC consolidation were taken in consideration. During monolithic sintering the SPS equipment presented instability on the cooling system complicating the sintering process, when 1750°C or higher temperature was reached, a decision to continue using only 1650°C and 1700°C was made, discarting the 1750°C sintering temeprature for all further tests. The most important parameters on this process are the temperature and fiber volume fraction since the heating rate, holding time and pressure will remain constant.

For the samples consolidated by spark plasma sintering; no additives were used and no prior cold pressing was made. Table 6 presents the sintering parameters used, the experiments were sintered at two different temperatures 1650°C and 1700°C, with a different combination of SiC fiber plies, the same pressure of 100 MPa, and constant heating rate of 100°C/min for all samples was used. A 1.0 gram target powder was used for all the samples homogeneously distributed among the fiber plies, the final sample measurements were disks of 20 mm diameter and 1.0-1.3 mm thick, depending on the fiber content and sample shrinkage after sintering.

The samples consolidated by hot press were fabricated at General Atomics; no additives were used and no prior cold pressing. Table 7 presents the sintering parameters

used, the pressure of 20 MPa and 1800°C in temperature were kept constant on all the samples. The heating rate and holding time are kept confidential for privacy reasons. The specimens were made on a bigger size die, for that reason the final sample measurements were disks of 50 mm diameter and 1.0-1.3 mm thick, depending on the fiber content and sample shrinkage after sintering.

3.4. SiC/SiC Density measurements

After consolidation, the density was calculated using the Archimedes' method. Table 6 and Table 7 present the density results obtained by varying the fiber volume fraction and temperature on the samples sintered by SPS and HP, respectively. Sample 12 suffered from imperfections during the sintering process and will be discarded from all further tests.

Table 6. Sintering parameters and density values for SiC/SiC fiber reinforced composites consolidated by SPS.

Sample	Temperature (°C)	Pressure (MPa)	Heating Rate (°C/min)	Holding Time (min)	Number of Plies	Fiber Volume Fraction	Density (g/cm^3)	Percentage (%)	Density Average (%)
1	1650	100	100	5	2	31.51%	3.041	94.74 ±0.46	94.14 ±0.98
2	1650	100	100	5	2	31.51%	2.960	92.19 ±0.90	
3	1650	100	100	5	3	40.83%	2.984	92.96 ±0.88	92.33 ±0.74
4	1650	100	100	5	3	40.83%	2.968	92.46 ±0.68	
5	1650	100	100	5	4	47.92%	2.868	89.33 ±0.31	90.55 ±1.41
6	1650	100	100	5	4	47.92%	2.946	91.77 ±0.78	
7	1700	100	100	5	2	31.51%	3.046	94.89 ±0.39	96.14 ±1.41
8	1700	100	100	5	2	31.51%	3.124	97.31 ±0.78	
9	1700	100	100	5	3	40.83%	2.996	93.34 ±0.74	94.96 ±1.95
10	1700	100	100	5	3	40.83%	3.100	96.58 ±1.16	
11	1700	100	100	5	4	47.92%	3.057	95.23 ±0.34	95.23 ±0.34
12	1700	100	100	5	4	47.92%	~	~	

Pure SiC Nanopowder (45-65nm) & SiC fiber (550nm PyC Coating)

The densification of SiC/SiC composites sintered by SPS and HP was dependent on fiber volume fraction and temperature. The sintering parameters for the composite samples used for each sintering technique are presented in **Table 6** and **Table 7**.

Table 7. Sintering parameters and density values for SiC/SiC fiber reinforced composites consolidated by HP.

Sample	Temperature (°C)	Pressure (MPa)	Heating Rate (°C/min)	Holding Time (min)	Number of Plies	Fiber Volume Fraction	Density (g/cm^3)	Percentage (%)
13	1800	20	15	-	2	25.2%	2.837	88.38 ±0.71
14	1800	20	15	-	3	41.5%	2.785	86.76 ±1.12
15	1800	20	15	-	4	49.3%	2.739	85.32 ±0.93

Pure SiC Nanopowder (45-65nm) & SiC fiber (550nm PyC Coating)

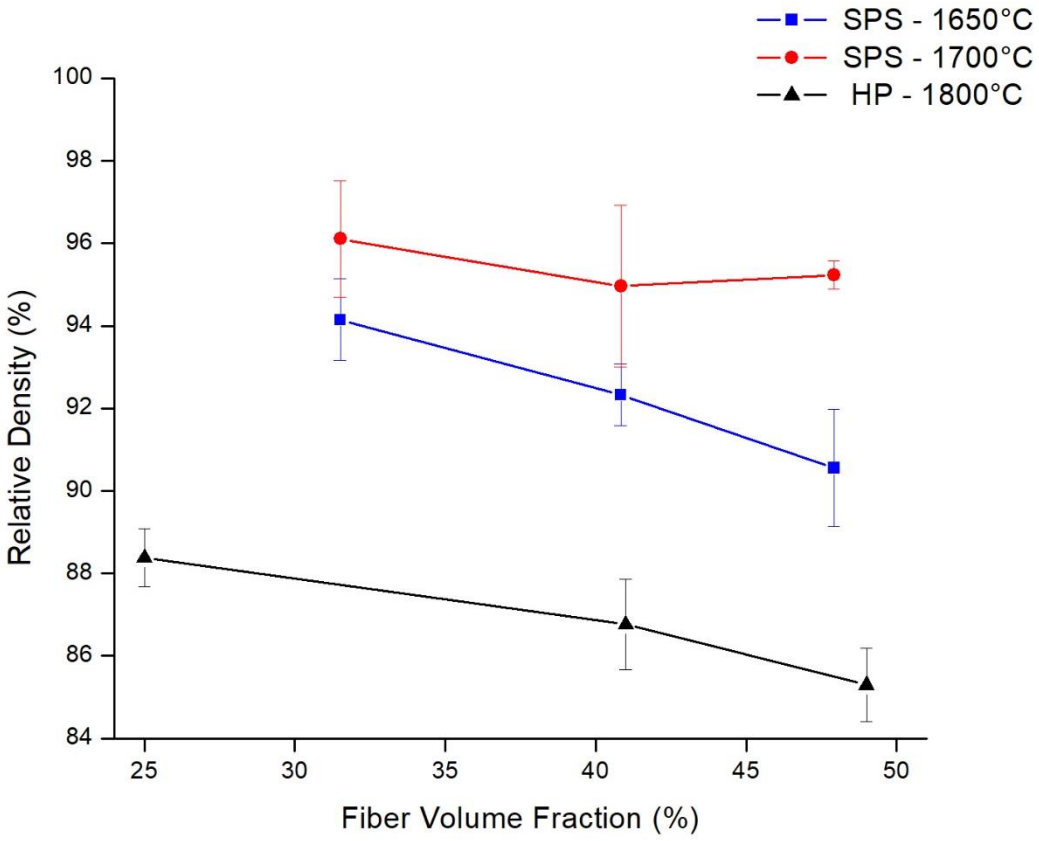

Figure 30. Effect of fiber volume on the relative density of samples sintered by SPS and HP.

The effect of fiber volume fraction on the relative density of the SPS and HP sintered composites is shown in **Figure 30**. Generally, the composites exhibit a decrease in relative density as the volume fraction of fibers increases, correlating well with the findings of other authors on similar materials [100, 101]. The composites sintered at 1700°C with lower fiber volume fraction presented an averaged higher relative density of 96.14% (see sample 7-8 in **Table 6**), compared to composites with higher volume fraction, experiencing a slightly lower relative density of 95.2% (see sample 11 in **Table 6**). At higher fiber content, the composites

exhibited a lower density due to the reduced infiltration of SiC nanopowder into the SiC fibers, consequently increasing the open porosity [102]. The reduction in density with fiber inclusion can be compensated by increasing the applied driving force (such as temperature and pressure), which enhances the infiltration of the SiC powders, as suggested by Shimoda *et al*. [Shimoda (2009)].

By comparing both sintering temperatures for the SPS technique, the effect of sintering temperature on the relative density of the samples was shown (see **Figure 30)**. At lower sintering temperature (1650°C), the relative density was lower compared to samples sintered at 1700°C. The diffusion process is promoted at a higher temperature, enhancing the mass transport mechanisms, resulting in a homogeneous microstructure, density increase, and porosity reduction [Noviyanto, 2011].

Our results show that SPS is a more effective SiC/SiC sintering method compared to HP. The SPS sample 8 in **Table 6**, showed a higher relative density (about 97.3%), compared to the HP sample 13 in **Table 7** (88.38%), at similar low fiber volume fraction. This can be attributed to the significant contribution of using higher pressure and electric current during the SPS sintering. It is clear, that the higher pressure of the SPS process (100 MPa) has a beneficial effect on particle rearrangement and the destruction of powder agglomerates, influencing the driving force for sintering [Garay, 2010]. In contrast, HP process is limited to 20 MPa due to the potential damage caused to the fibers during the long processing time [Dong, 2003]. The composite consolidatied by SPS was benefited from the Joule heating effect resulting from the significant current passing through the powder particles and generating a self-heating, leading to a higher density compared to HP [[103], [104], Tokita,2006].

3.5. Microstructural Analysis of SiC/SiC composites

Microstructural analysis of the SPS samples was performed by SEM and it was determined that all the samples presented a similar microstructure. A representative sample (Sample 8) is illustrated in **Figure 31**. The matrix presented a densified microstructure with minimal porosity as shown in **Figure 31(a)**, although some small pores remained between the fibers, as illustrated in **Figure 31(b)**.

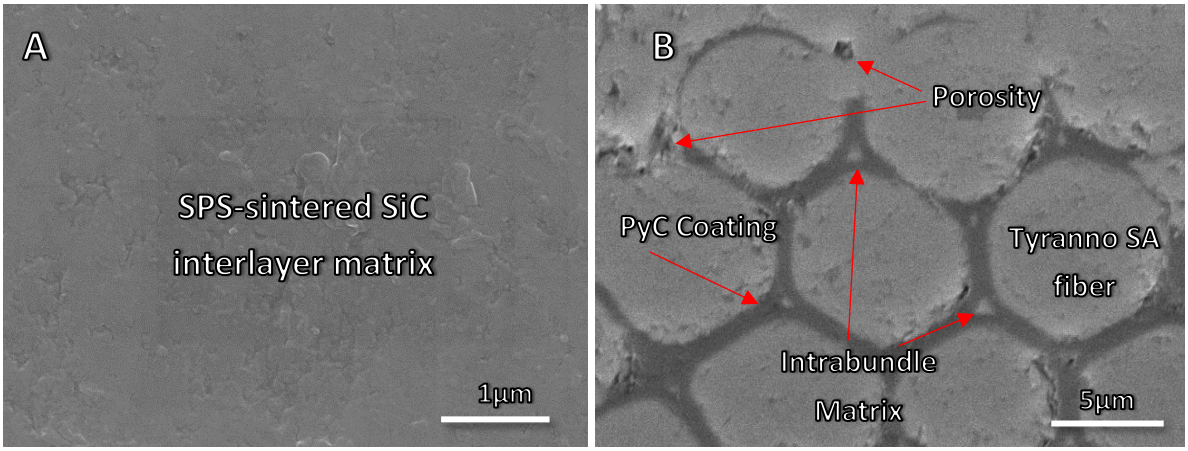

Figure 31. Scanning electron micrograph of (a) the polished surface of the matrix section of sample D presenting a uniform microstructure and low porosity, (b) the polished cross-section of the SiC fiber morphology and PyC coating of sample D.

The fracture surfaces of the SPS samples exhibited fiber pullout, which was identified as the primary fracture mechanism, as illustrated in **Figure 32(a)**. For the HP samples fiber pullout was also present, relatively more significant voids and signs of vertical cracks as presented in **Figure 32(b)**. These fracture characteristics may indicate a weaker fiber/matrix interphase bonding. The PyC layer present in the fibers was used as an interface coating between the matrix and the fiber, which protects the SiC fibers from the high-temperature conditions during processing [[105]].

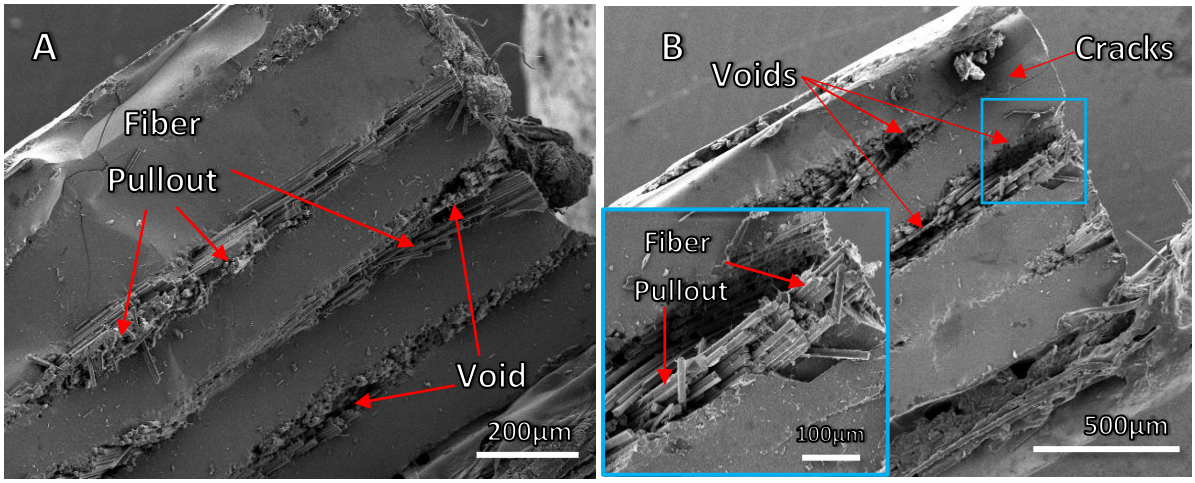

Figure 32. Scanning electron micrographs of fractured surfaces in samples sintered by (a) SPS (sample E) and (b) HP (sample H). Fiber microstructure of samples after (c) SPS (sample E) and (d) HP (sample H) sintering.

3.6. Mechanical Performance of SiC/SiC composite material

The bending test was performed on the sintered materials to determine if the fiber reinforcement can improve the deflection of the SiC composites during loading and determine the flexural strength. Three-point bending test was performed on the SiC matrix composite according to the ASTM C1341 "Standard Test Method for Flexural Properties of Continuous Fiber-Reinforced Composites Advanced Ceramic", the flexural strength was calculated from this data, and the resulting fractured samples were analyzed using SEM and microhardness.

Table 8 present the corresponding sintering conditions for each SPS sample with the achieved density, fiber volume fraction, thickness and flexural strength. The strain rate used was in the range (1.2-1.45) $x10^{-03}$ and a constant crosshead rate displacement of 0.0427 mm/s. As noticed, the samples 2.1 & 2.2 presented abnormally lower flexure strength due to imperfection on the sintering process while sample 10.1 &10.2 presented the highest overall strength values. There is a visible difference between the samples sintered at 1650°C and 1700°C; we see higher flexure values for the predicted temperature suggested by the SiC monolithic sintering.

Table 8. Summary of sintering conditions proposed for step 3, density and flexure strength results.

Sample	Temperature (°C)	Pressure (MPa)	Number of Plies	Fiber Volume Fraction	Density (g/cm^3)	Percentage (%)	Thickness (mm)	Flexural Strength (MPa)
1.1	1650	100	2	31.5%	3.04	94.74 ±0.46	1.30	156.1
1.2	1650	100	2	31.5%	3.04	94.74 ±0.46	1.30	285.5
2.1	1650	100	2	31.5%	2.96	92.19 ±0.90	1.38	20.5
2.2	1650	100	2	31.5%	2.96	92.19 ±0.90	1.38	6.3
3.1	1650	100	3	40.8%	2.98	92.96 ±0.88	1.47	150.3
3.2	1650	100	3	40.8%	2.98	92.96 ±0.88	1.47	245.6
4.1	1650	100	3	40.8%	2.97	92.46 ±0.68	1.26	306.1
4.2	1650	100	3	40.8%	2.97	92.46 ±0.68	1.32	326.5
5.1	1650	100	4	47.9%	2.87	89.33 ±0.31	1.19	186.4
5.2	1650	100	4	47.9%	2.87	89.33 ±0.31	1.20	268.6
6.1	1650	100	4	47.9%	2.95	91.77 ±0.78	1.35	280.6
6.2	1650	100	4	47.9%	2.95	91.77 ±0.78	1.30	258.9
7.1	1700	100	2	31.5%	3.05	94.89 ±0.39	1.28	289.6
7.2	1700	100	2	31.5%	3.05	94.89 ±0.39	1.27	226.0
8.1	1700	100	2	31.5%	3.12	97.31 ±0.78	1.20	288.3
8.2	1700	100	2	31.5%	3.12	97.31 ±0.78	1.18	235.5
9.1	1700	100	3	40.8%	3.00	93.34 ±0.74	1.25	291.9
9.2	1700	100	3	40.8%	3.00	93.34 ±0.74	1.23	252.2
10.1	1700	100	3	40.8%	3.10	96.58 ±1.16	1.33	350.9
10.2	1700	100	3	40.8%	3.10	96.58 ±1.16	1.33	335.8
11.1	1700	100	4	47.9%	3.06	95.23 ±0.34	1.30	328.4
11.2	1700	100	4	47.9%	3.06	95.23 ±0.34	1.32	276.3

Pure SiC Nanopowder (45-65nm) & SiC fiber (550nm PyC Coating)

There is an interesting phenomenon, there it seems not to be a direct correlation between density and flexure strength some materials have a higher density but even though the flexure values are lower, or even the same sample sintered at the same conditions didn't achieve a similar flexure value, this can be attributed to different reasons:

- The density measurements are not completely accurate because it does not consider the internal porosity of the material.

- Flexure strength values are not completely dependent of just the density of material but instead is a group of circumstances as the microstructure, grain size, imperfections or second phases developed during the sintering that is working together.
- The flexural strength of a ceramic composite is not a deterministic quantity but can change values from one specimen to another. This variability is grounded on the inherent differences in ceramic composites made with fiber reinforcement. Variables include property/morphology variations in fibers, matrix, and interface coatings, as well as discrepancies in the architecture, reinforcement volume fraction, sample assembly and density in the composite. Such variations can occur spatially within the same test sample, as well as between different test specimens [106].

A "propagation of errors" study [107] showed that the measurement of sample's thickness is a serious source of variability because flexure and elastic modulus values are calculated by equations which use thickness values. Additionally, the thickness values are usually the smallest dimension, for this reason, it is the most vulnerable to experimental variation between samples and between laboratories.

Taking in consideration the previous information, to maintain repeatability and reduced variability in the flexure results, on this study only the samples from each category with thickness ~1.3mm will be taken in consideration for further experiments. The new table of flexure performance data for the analysis of SPS samples is presented in Table 9. The samples with V_f = 31.5% sintered at 1650°C, showed the lowest strength which was approximately 30-40% lower than the same ceramic composite material with V_f = 31.5% sintered at 1700°C. The flexure results for HP samples is presented in Table 10.

Table 9. Flexure results and sintering conditions corresponding to SPS samples under new conditions to reduce errors.

Sample	Temperature (°C)	Pressure (MPa)	Number of Plies	Fiber Volume Fraction	Density (%)	Thickness (mm)	Flexural Strength (MPa)	Strength Average (MPa)
1.1	1650	100	2	31.5%	94.14 ±0.98	1.30	156.1	220.79
1.2						1.30	285.5	
4.1			3	40.8%	92.33 ±0.74	1.26	306.1	316.30
4.2						1.32	326.5	
6.1			4	47.9%	90.55 ±1.41	1.35	280.6	269.75
6.2						1.30	258.9	
7.1	1700	100	2	31.5%	96.14 ±1.41	1.28	289.6	257.80
7.2						1.27	226.0	
10.1			3	40.8%	94.96 ±1.95	1.33	350.9	343.36
10.2						1.33	335.8	
11.1			4	47.9%	95.23 ±0.34	1.30	328.4	302.38
11.2						1.32	276.3	

Pure SiC Nanopowder (45-65nm) & SiC fiber (550nm PyC Coating)

Table 10. Flexure results and sintering conditions corresponding to HP samples.

Sample	Temperature (°C)	Pressure (MPa)	Number of Plies	Fiber Volume Fraction	Density (%)	Flexural Strength (MPa)	Strength Average (MPa)
13.1	1800	20	2	25.2%	88.38 ±0.71	167.76	169.85
13.2						171.93	
14.1			3	41.5%	86.76 ±1.12	238.91	228.66
14.2						218.41	
15.1			4	49.3%	85.32 ±0.93	187.00	181.24
15.2						175.48	

Pure SiC Nanopowder (45-65nm) & SiC fiber (550nm PyC Coating)

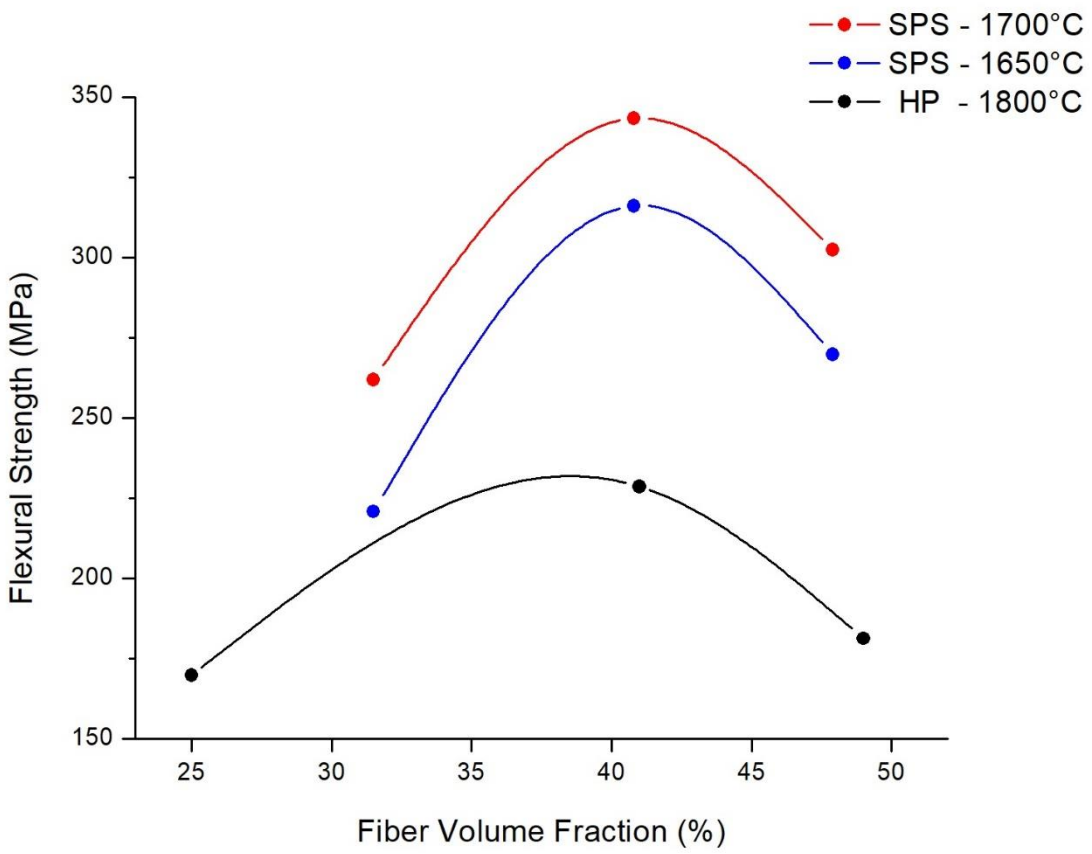

Figure 33. Flexure strength results in terms of fiber volume fraction for step 3 data.

The mean flexural strength values as a function of fiber volume fraction % for HP and SPS sintered samples is presented in **Figure 33**. The strength is ruled by the SiC fibers present in the composites [108], a rise in the modulus is caused by the reinforcement effect of SiC fibers, which avoids early sliding of the SiC matrix phase [109]. When fiber volume fraction is near 40%, homogeneous spreading of fibers in the composite is obtained and the maximum strength of the composite is achieved at 343.36 MPa for SPS samples sintered at 1700°C. This is accredited to a higher modulus of Tyranno SA SiC fibers than that of ceramic SiC matrix; stress transmission can occur near the fibers. Therefore, the effect of crack development and deflection in different directions is more dominant than the effect in crack propagation in just

one direction; if the material has multiple paths to distribute the applied load, the fibers can successfully contribute in the stress transfer. As we see on **Figure 33**, at higher fiber content (~50% fiber volume fraction) there is a decrease on flexural strength this can be attributed to a lower impregnation of the SiC fibers in the ceramic matrix, and the increased volume of fibers contribute to an agglomeration, and stress transfer is blocked [110]. Large amounts of isolated fiber to fiber contact and matrix fracture at the surface of the fiber agglomerate become the failure mechanism in this case [111].

The 3-point bending test load-displacement curve for all the fiber reinforced samples presented on Table 9 and Table 10 are shown in **Figure 34** for SPS samples and **Figure 35** for HP samples respectively. As is well known, stress-strain curves of the flexural test can give relevant information. The overall flexure strength of SPS sintered samples was higher than HP samples. However, material withstood only a small amount of strain before exhibiting brittle failure similar to a monolithic ceramic material.

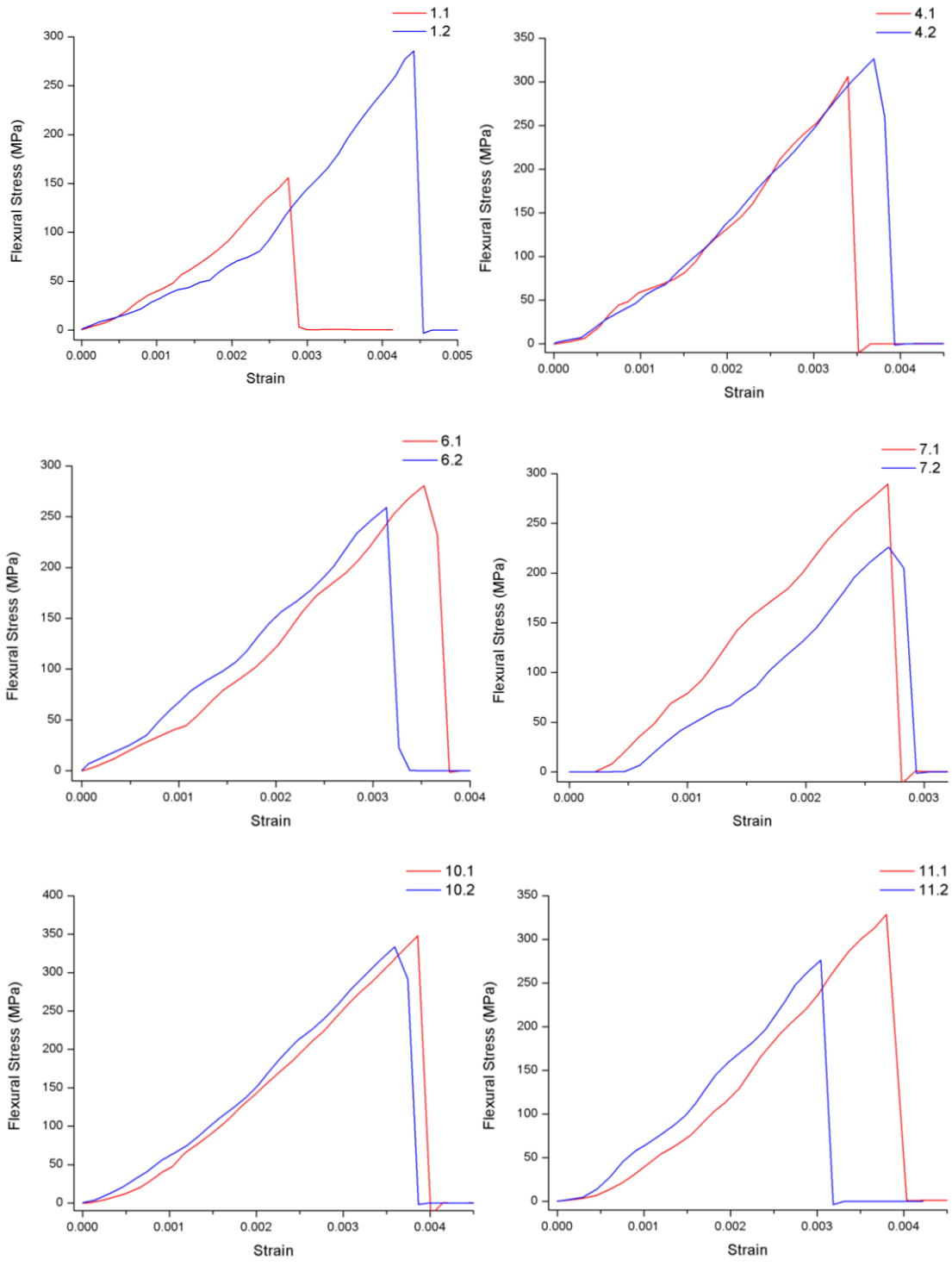

Figure 34. Stress-strain relationship curves for samples on table 9.

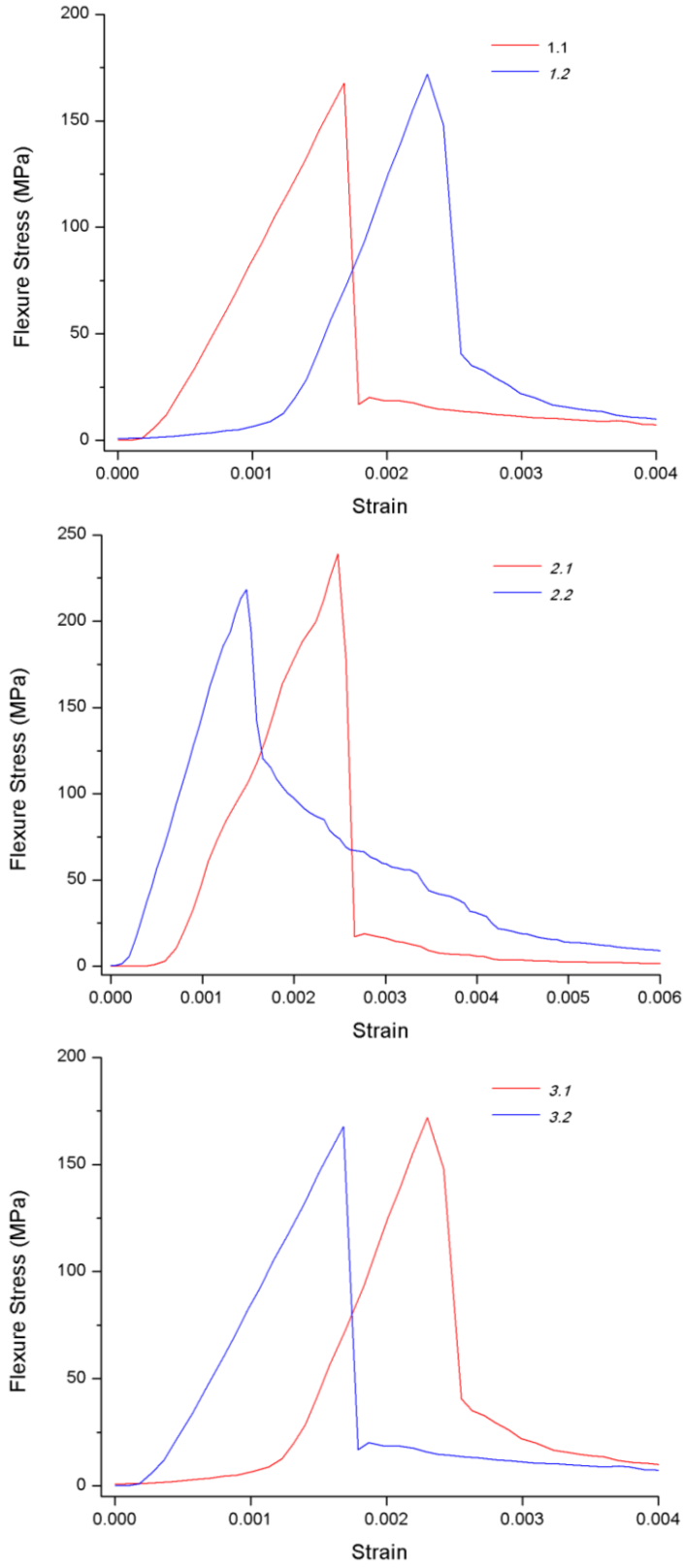

Figure 35. Stress-stain relationship of curve, for samples on table 10.

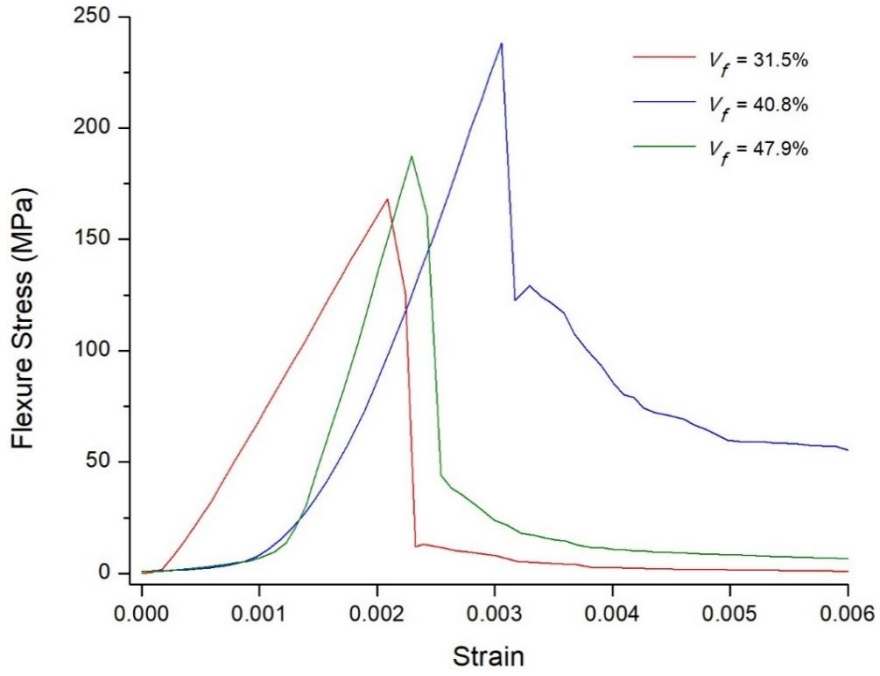

Figure 36. Typical stress-strain curves of SiC/SiC sintered by HP during the flexural test.

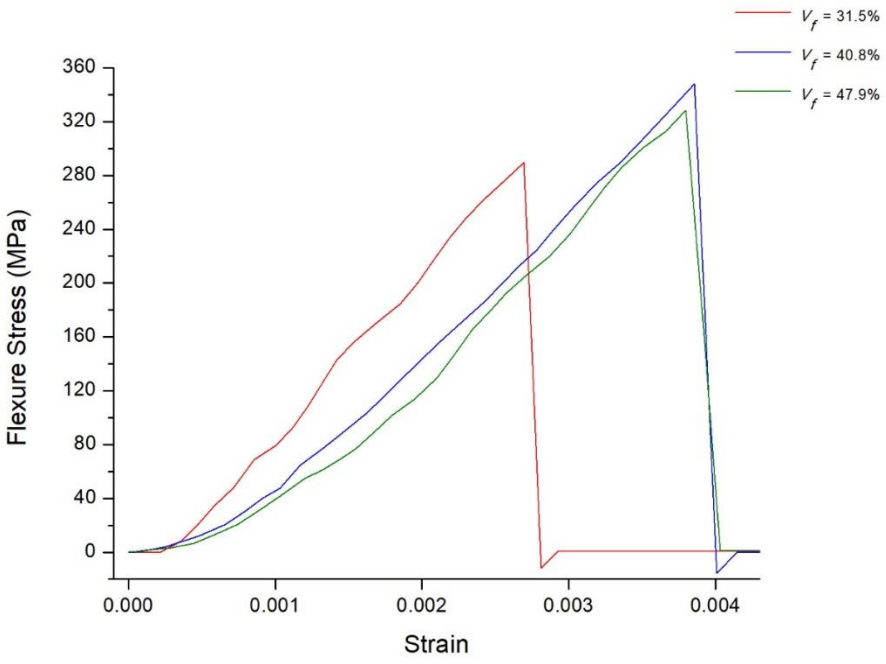

Figure 37. Typical stress-strain curves of SiC/SiC sintered by SPS during the flexural test.

A summary of the different types of stress-strain curves presented on the SiC/SiC SPS and HP sintered material at different fiber volume fraction are shown in **Figure 36** and **Figure 37**. The strain or elongation was significantly the same in all SPS and HP species.

The HP sintered samples, presented 3 different behaviors (**Figure 36**), the first curve at 25.2% fiber content, presented a sudden fall after reaching the maximum flexure strength with little yielding, a cracking noise was heard when the fracture happened, suggesting a typical brittle fracture behavior (without fiber pull-out). The second curve with 41.5% fiber content, shows a gradual decrease after reaching the maximum force, meaning that the crack propagation is happening stably and continuously over the specimen. The force is distributed over a larger span, which can develop more crack surface and deflect a noncatastrophic fracture mode. With the increase in displacement of the fiber laminates, more parts of the matrix and laminates reach ultimate strength, but the overall strength is not enhanced during the plastic deformation. The third curve with 49.3% fiber content, is associated with uneven crack propagation as shown on the first curve , as we mentioned above, we can attribute this phenomenon to the fibers that are not adequately impregnated by the ceramic matrix due to much higher fiber volume fraction, producing pores and voids between the fibers blocking the stress transfer. Therefore, the reinforcing effect of SiC fibers over the Ceramic matrix is limited by a large extent.

On the other hand, the SPS samples fracture behavior on **Figure 37**, presented a catastrophic failure mode, where a substantial proportion of the fibers break in the wake of the first matrix crack as it extends, the ultimate strength is limited by the growth of a single dominant crack. This kind of failure is characterized by an initial linear elastic response; the

properties can be estimated by the fundamental properties of the material and the fiber volume fraction. The damage extends predominately of multiple matrix cracking; the cracks are likely to debond the fiber/matrix interface and cause slip at the interface across the width of the specimen, with the increase of the loading the cracks can cover the entire cross-section of the specimen. It is likely that the fibers are debonded after the cracking is done[112], the unloading behavior in the strain range indicates significant presence of the fiber/matrix interfacial sliding until fracture, dominated by the localized fiber failure of the composite.

As mentioned on chapter 2.4 Sample Preparation section, the SiC disk was cut in two strips with 19mm X 4mm in dimensions, to facilitate the further mechanical tests, these pieces were supported on epoxy and continued with polishing.

The microhardness data presented in Table 11 shows all the values collected for the samples, which were taken using Vickers hardness tester. **Figure 38** plots the hardness information and shows the relationship between hardness values and sintering temperature for samples at different fiber volume fraction.

All the samples presented error scattered values ranging from 0.1-0.6 GPa**.** By comparing the hardness results of sintered samples for the same temperature and various fiber content, it was proven that there is little variation of hardness between samples with the same sintering conditions regardless of the fiber content. However, with the use of different processing techniques and variation of sintering temperature, the density is modified, which affected the hardness results, as presented in **Figure 39**. These results correlate well with Novitskaya *et al*. [Novitskaya (2018)], where it was demonstrated that the microhardness results of SiC/SiC were independent of the fiber volume fraction of the composites produced

by HP. The difference in hardness values at different sintering temperatures was a direct consequence of the variation in density values. The SPS samples did not suffer a significant decrease in hardness compared to monolithic β-SiC (~27.7 GPa) [113]. Sample 10.1 and 10.2 (produced by SPS) had a Vickers hardness value of 26.0 GPa, while the value for Sample 14.1 and 14.2 (produced by HP) was found to be 21.2 GPa, which correlates with the 21.9 GPa value for the β-SiC phase produced by a similar sintering technique [114].

Table 11. Microhardness results for SPS samples

Sample	Temperature (°C)	Pressure (MPa)	Number of Plies	Fiber Volume Fraction	Density (%)	Microhardness (GPa)	Microhardness Average (GPa)
1.1 1.2	1650	100	2	31.5%	94.14 ±0.98	22.83 ±0.36 22.66 ±0.37	22.75 ±0.35
4.1 4.2			3	40.8%	92.33 ±0.74	23.81 ±0.32 24.25 ±0.64	24.03 ±0.53
6.1 6.2			4	47.9%	90.55 ±1.41	22.61±0.43 22.74 ±0.57	22.68 ±0.48
7.1 7.2	1700	100	2	31.5%	96.14 ±1.41	24.41 ±0.53 23.98 ±0.38	24.20 ±0.49
10.1 10.2			3	40.8%	94.96 ±1.95	25.72 ±0.37 26.33 ±0.19	26.02 ±0.43
11.1 11.2			4	47.9%	95.23 ±0.34	25.27 ±0.34 25.59 ±0.83	25.43 ±0.62

Pure SiC Nanopowder (45-65nm) & SiC fiber (550nm PyC Coating)

Table 12. Microhardness results for HP samples.

Sample	Temperature (°C)	Pressure (MPa)	Number of Plies	Fiber Volume Fraction	Density (%)	Microhardness (GPa)	Microhardness Average (GPa)
13.1 13.2	1800	20	2	25.2%	88.38 ±0.71	20.43 ±0.15 20.44 ±0.33	20.43 ±0.23
14.1 14.2			3	41.5%	86.76 ±1.12	21.30 ±0.27 21.18 ±0.28	21.24 ±0.26
15.1 15.2			4	49.3%	85.32 ±0.93	20.41 ±0.30 20.19 ±0.37	20.31 ±0.33

Pure SiC Nanopowder (45-65nm) & SiC fiber (550nm PyC Coating)

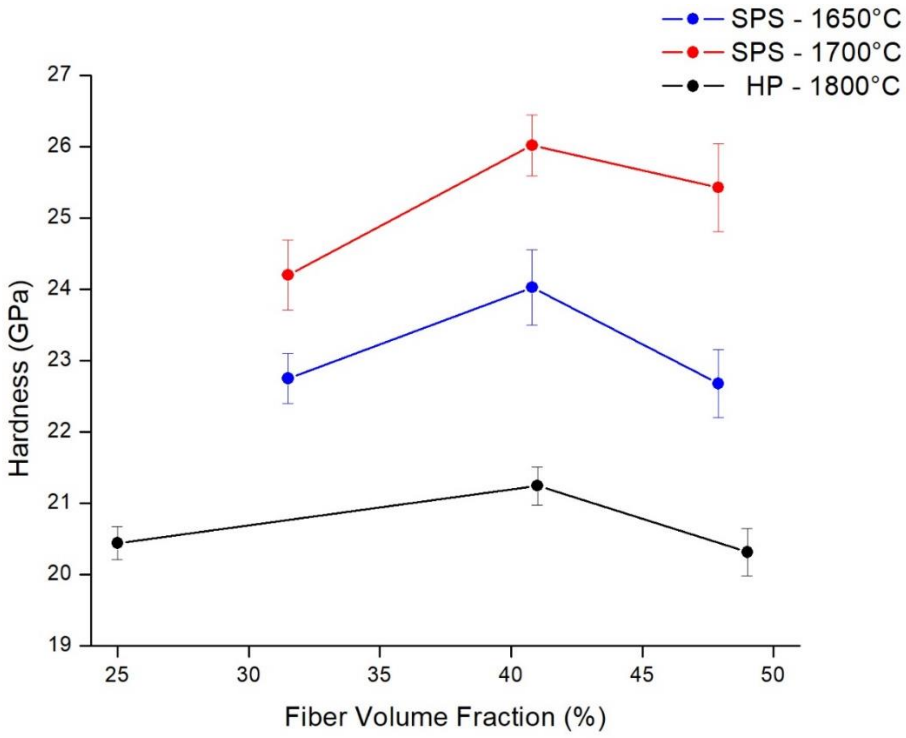

Figure 38. The relationship between hardness at different fiber volume fractions.

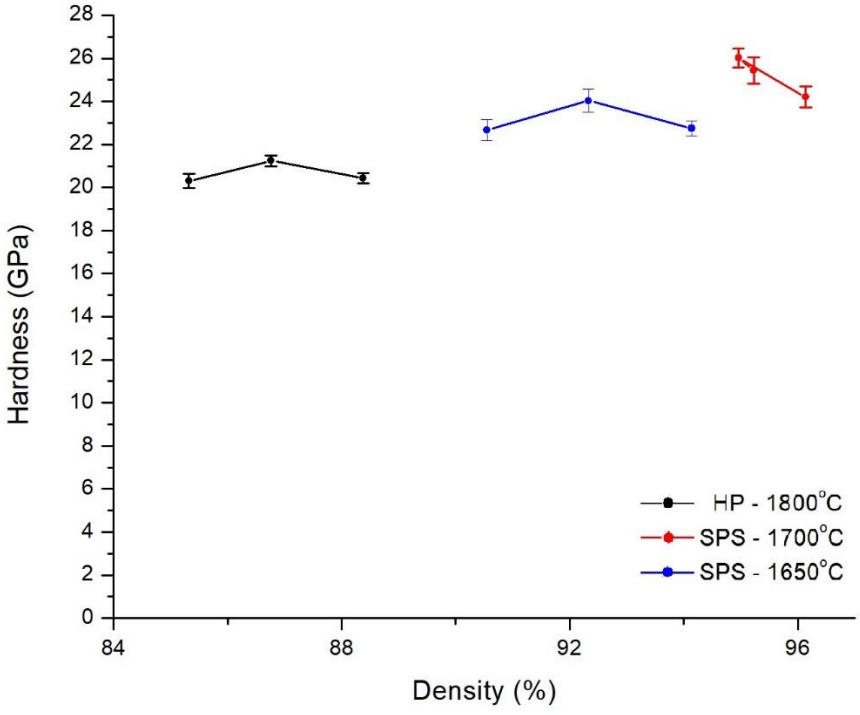

Figure 39. Effect of density on the hardness values of samples sintered by SPS and HP.

3.7. X-Ray diffraction Analysis and β→α SiC phase transformation

X-ray diffraction pattern of the β-SiC starting powder is illustrated in **Figure 40**, presenting a broad peak at 33.7° degrees 2θ near the highest intensity peak of β-SiC 35.6° degres 2θ . Computer simulations and high-resolution transmission electron microscopy (HRTEM) characterization was performed by Pujar *et al*. [115, 116]. It was concluded that the signal at 33.7° corresponds to β-SiC stacking faults, and not to the presence of minor amounts of other phases in the SiC powder. Summarizing all above, it was concluded that our raw β-SiC powder did not show any sign of impurities or traces of isolated α-SiC phases.

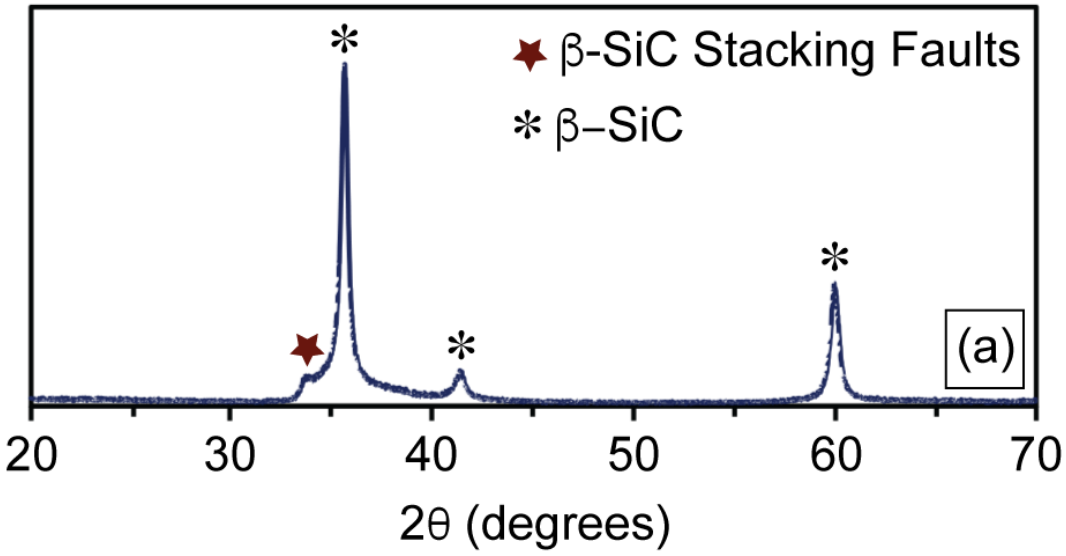

Figure 40. X-ray diffraction pattern of the β-SiC starting powder showing the presence of stacking faults.

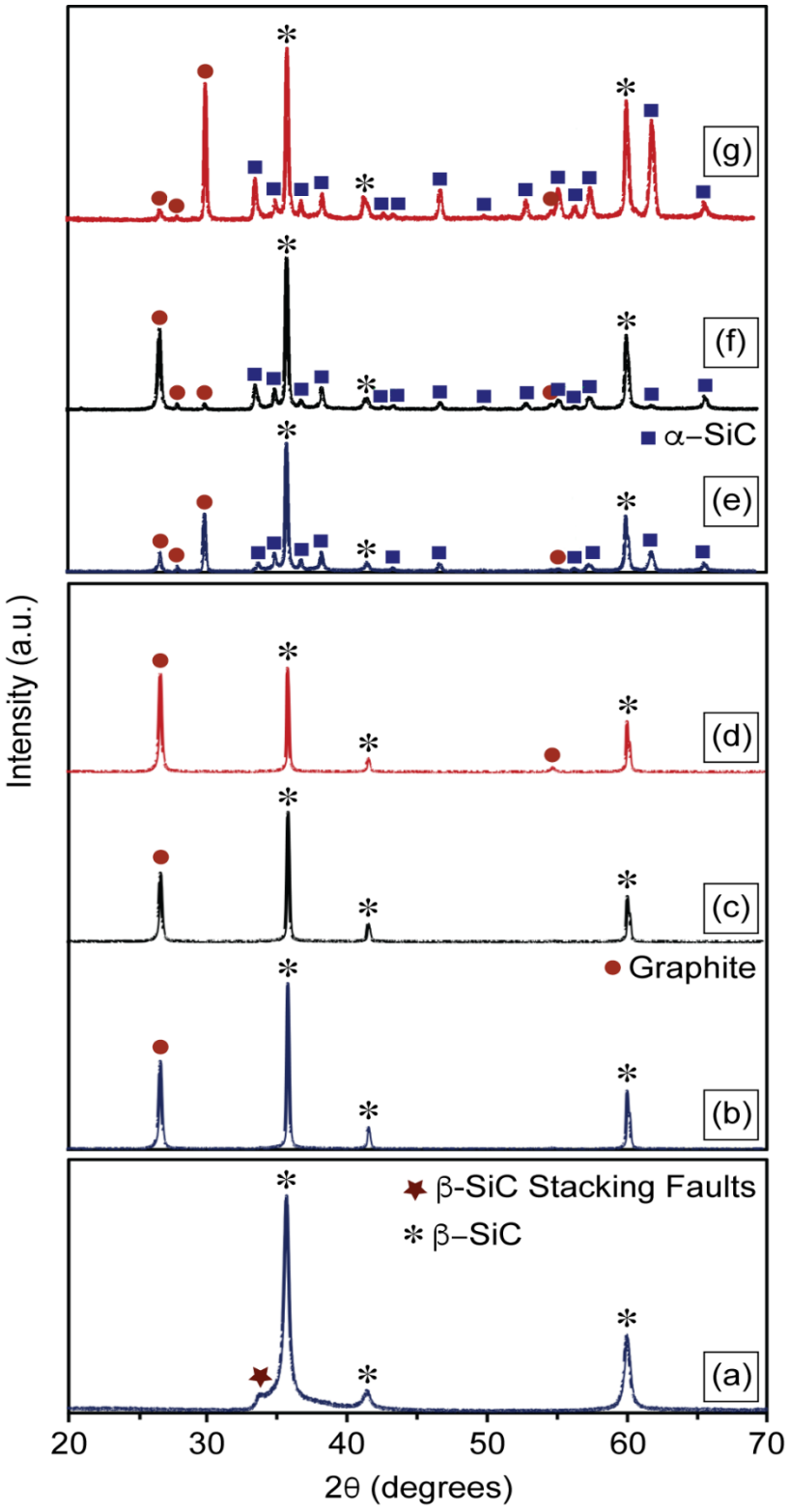

Figure 41. XRD Results of samples sintered at different fiber volume fractions.

Furthermore, the XRD patterns of the samples sintered by SPS and HP techniques were analyzed to verify if the SiC β→α phase transformation took place during the sintering processes. **Figure 41** summarizes the XRD patterns of the starting β-SiC nanopowder, samples sintered at 1700°C by SPS (**Table 11**, samples 7.1, 10.1, 11.1), and samples sintered by HP (**Table 12**, samples 13.2, 14.1, 15.1) for different fiber volume fractions. The XRD pattern of the SPS samples showed the presence of only one phase, the β-SiC polytype (PDF #00-029-1129) crystal structure similar to diamond [117], presenting the most dominant peaks at approximately 35.6°, 41.4°, and 60° degrees 2θ. Several peaks from the graphite foil (PDF #01-089-8487) were also detected at 2θ = 26.8° and 54.9°. While the samples sintered by SPS consisted only of the β-SiC phase, samples sintered by HP technique exhibited a mixture of β-SiC and α-SiC, with the latter peaks of much higher intensity. The α-SiC polytypes 4H (PDF #00-029-1127) and 6H (PDF #00-029-1131) from the HP samples can be recognized from their isolated peaks approximately at 33.5°, 34.2°, 36.4°, 38.9°, 46.3°, 53.3°, 57.2°, 60.7°, 61.3°, 65.6°. The presence of the α-SiC polytypes (4H and 6H) proves that the β to α transformation took place during HP sintering. The phase concentration changed drastically from a complete β-SiC phase on the SPS samples to ~19% β-SiC and ~81% α-SiC on the HP sintered samples. The phase concentration in the mixture was calculated by the direct comparison method, which makes a quantitative analysis by comparing the experimental highest intensity peak (I/I_0 = 100%) of β-SiC at 2θ = 35.62° to the highest intensity peak (I/I_0 = 100%) of α-SiC at 2θ = 36.48° [118, 119, 120].

The fact that α-SiC peaks are only present in the XRD patterns of the HP sintered samples can be explained by the processing advantages of SPS over HP. The lower processing temperature (1700°C) during SPS sintering is commonly associated with a retardation on SiC

phase transformation [[121], Munir, 2006], compared to HP samples manufactured at 1800°C were a significant surface diffusion occurs, accelerarting the β to α phase transformation [[122]]. The sintering is also benefited by the high heating rate of SPS (100°C/min) compared to HP (15°C/min), which reduces the time the material stays at high temperature, minimizing the new phase nucleation drastically [Munir, 2006]. Finally, the higher uniaxial pressure applied during SPS sintering, enhance the stability of the β phase, retarding the SiC phase transformation [Sugiyama, 2001].

4. Summary of Accomplishments and Conclusion

This study explored the sintering behavior of SiC/SiC fiber reinforced composite sintered by SPS and a comparison in microstructure and mechanical properties with HP sintered samples.

- SPS proved to be the preferred composite fabrication route for SiC/SiC composites, due to the faster processing time, higher pressure and high relative density (96.1%), compared to HP sintered samples (88.3%).
- Generally, the composites exhibited a decrease in relative density as the volume fraction of fibers increases as a consequence of the reduced infiltration of SiC nanopowder into the SiC fibers, which increase the open porosity of the samples.
- X-ray diffraction analysis was performed on HP and SPS sintered samples. β-SiC was the only phase found in the diffraction patterns of the SPS samples. A semi-quantitative analysis was performed on the HP sintered samples showing a predominant concentration (~81%) of α-SiC, compared to β-SiC (~19%), proving that the β to α transformation took place only during the HP consolidation. The absence of α phase in the SPS samples is

attributed to the processing benefits of this technique over HP, namely lower sintering temperature, shorter processing time, higher heating rate, and higher pressure.

- It was verified that both SPS and HP SiC/SiC composites suffered from a reduction in relative density as the fiber loading increased. This behavior was attributed to the reduced interconnectivity of the SiC fibers with the surrounding ceramic matrix at the higher fiber loadings. Both techniques presented fiber pullout as the main fracture mechanism. HP produced samples presented longer detached fibers from the matrix compared to the SPS produced ones, indicating a weaker matrix impregnation between the fibers.
- Microhardness values were determined for the samples, demonstrating an independent relationship between the hardness and the fiber volume fraction. The lower microhardness values of HP samples compared to SPS, can be attributed to the lower density values obtained during HP processing.

- The Flexural strength of the SPS sintered samples presented a 343.36 MPa value and the failure behavior showed elastic response in the beginning, and then a non-linear behavior near the peak load, followed by a sudden decreasing after the maximum load. These demonstrate a catastrophic and early failure mode, which is responsible for the brittle failure with in the specimens. In contrast, the curves for the HP sintered samples, especially for sample at 40.8% fiber content presented a 228.6 MPa flexural strength, but with a standard toughened fracture behavior. When the load reaches its maximum value, it will drop off gradually. The strain is larger compared with the SPS samples. These indicate that abundant of fracture energy has been exhausted and the toughness has been improved prominently. Even though the SPS samples presented higher flexural strength, it also presented brittle behavior, it can be

attributed to the strong interfacial bond of the SiC fiber and SiC matrix, which suppressed the possible interface debonding, cracks deflection, cracks branching and fiber bridging.

SPS demonstrated to be a reliable sintering method to consolidate SiC/SiC composites with high relative density (96.1%), uniform internal microstructure, hardness values similar to pure β-SiC, without suffering from the β→α phase transformation during sintering. There are still opportunity in the development of this material, providing an opportunity to design a ceramic material with the mechanical advantages of a fiber reinforced composite and the property benefits of monolithic β-SiC.

5. References

[1] P. Raback, R.Nieminen "Thermodynamic considerations on the role of hydrogen in sublimation growth of silicon carbide," *Journal of the Electrochemical Society*, 144 [3] 1024-1027 (1997).

[2] P. Raback, R.Nieminen, "A coupled finite element model for the sublimation growth of SiC," *Materials Science Forum,* 65, 264-268 (1998).

[3] R. Cheung, "Silicon Carbide Microelectromechanical Systems for Harsh Environments," (Imperial College Press, 2006).

[4] H. Morkoc, S. Strite, G. Gao, M. Lin, B. Sverdlov, M. Burns, "Large-band-gap SiC, III-V nitride, and II-VI ZnSe-based semicondictor device technologies," *Journal of Applied Physics,* 76 [3] 1363-1398 (1994).

[5] O. Kordina, "Growth and Characterization of Silicon Carbide Power Device Material", (Linköping University: PhD thesis, 1994)

[6] WY. Ching, YN. Xu, P. Rulis, L. Ouyang, "The Eletronic Structure and Spectroscopic properties of 3C, 2H, 4H, 6H, 15R and 21R polymorphs of SiC," *Materials Science and Engineering A,* 422 [2] 147-156 (2006).

[7] AH. Heuer, GA. Fryburg, LU. Ogbuji, "β→ α transformation in polycrystalline SiC: I, microstructural aspects," *Journal of the American Ceramic Society,* 61, 406-412 (1978).

[8] TE. Mitchell, LU. Ogbuji, AH. Heuer, "β→ α transformation in polycrystalline SiC: II, interfacial energetics," *Journal of the American Ceramic Society,* 61, 412-413 (1978).

[9] RJ. Xie, M. Mitomo, W. Kim, YW. Kim, "Phase Transformation and Texture in Hot-Forged or Annealed Liquid-Phase-Sintered Silicon Carbide Ceramics," *Journal of the American Ceramic Society*, 85 [2] 459-465 (2002).

[10] T. Nagano, H. Gu, K. Kaneko, GD. Zhan, "Effect of Dynamic Microstructural Change on Deformation Behavior in Liquid-Phase-Sintered Silicon Carbide with Al_2O_3–Y_2O_3–CaO Additions," Journal of the American Ceramic Society, 84, 2045-2050 (2001).

[11] GD. Zhan, M. Mitomo, YW. Kim, "Microstructural control for strengthening of silicon carbide ceramics," *Journal of the American Ceramic Society*, 82, 2924-2926 (1999).

[12] CW. Jang, J. Kim, SJL. Kang, "Effect of Sintering Atmosphere on Grain Shape and Grain Growth in Liquid-Phase-Sintered Silicon Carbide," *Journal of the American Ceramic Society,* 85, 1281-1284 (2002).

[13] YW. Kim, M. Mitomo, H. Emoto, "Effect of initial α-phase content on microstructure and mechanical properties of sintered silicon carbide." *Journal of the American Ceramic Society,* 81 [12] 3136-3140 (1998).

[14] Y. Zhou, H. Tanaka, S. Otani, "Low-temperature pressureless sintering of alpha-SiC with Al_4C_3-B_4C-C additions," *Journal of the American Ceramic Society,* 27, 1959-1964 (1999).

[15] Y. Shinoda, M. Yoshida, T. Akatsu, "Effect of amount of boron doping on compression deformation of fine-grained silicon carbide at elevated temperature," *Journal of the American Ceramic Society,* 87, 1525-1529 (2004).

[16] T. Yamamoto, H. Kitaura, Y. Kodera, T. Ishii, " Consolidation of Nanostructured β-SiC by Spark Plasma Sintering," *Journal of the American Ceramic Society,* 87, 1436-1441 (2004).

[17] R. Vassen, A. Kaiser, J. Förster, HP. Buchkremer, "Densification of ultrafine SiC powders," *Journal of Materials Science,* 31, 3623-3637 (1996).

[18] A. Maitre, AV. Put, JP. Laval, S. Valette, "Role of boron on the Spark Plasma Sintering of an alpha-SiC powder," *Journal of the European Ceramic Society,* 28, 1881-1890 (2008).

[19] Y. Zhou, K. Hirao, M. Toriyama, "Very Rapid Densification of Nanometer Silicon Carbide Powder by Pulse Electric Current Sintering," *Journal of the American Ceramic Society,* 83, 654-656 (2000).

[20] E. Novitskaya, S. Díaz-de-la-Torre, T.A. Esquivel-Castro, G.R. Dieguez-Trejo, A. Kritsuk, J.T. Cahill, and O.A. Graeve, "Current Assisted Extrusion of Metallic Alloys: Insight into Microstructure Formation and Mechanical Properties," *Materials Science & Engineering A*, 717, 62-67 (2018).

[21] J.T. Cahill, V.R. Vasquez, S.T. Misture, D. Edwards, and O.A. Graeve, "Effect of Current on Diffusivity in Metal Hexaborides," *ACS Applied Materials & Interfaces*, 9 [42] 37357-37363 (2017).

[22] J.T. Cahill, M. Alberga, J. Bahena, C. Pisano, R. Borja-Urby, V.R. Vasquez, D. Edwards, S.T. Misture, and O.A. Graeve, "Phase Stability of Mixed-Cation Alkaline-Earth Hexaborides," *Crystal Growth & Design*, 17 [6] 3450-3461 (2017).

[23] J.P. Kelly, S.M. Fuller, K. Seo, E. Novitskaya, V. Eliasson, A.M. Hodge, and O.A. Graeve, "Designing *In Situ* and *Ex Situ* Bulk Metallic Glass Matrix Composites from Marginal Glass Formers via Spark Plasma Sintering in the Super Cooled Liquid State," *Materials & Design*, 93, 26-38 (2016).

[24] J.P. Kelly and O.A. Graeve, "Mechanisms of Pore Formation in High-temperature Carbides: Case Study of TaC Prepared by Spark Plasma Sintering," *Acta Materialia*, 84, 472-483 (2015).

[25] O.A. Graeve, M.S. Saterlie, R. Kanakala, S. Diaz de la Torre, and J.C. Farmer, "The Kinetics of Devitrification of Amorphous Alloys: The Time-Temperature-Crystallinity Diagram Describing the Spark Plasma Sintering of Fe-Based Metallic Glasses," *Scripta Materialia*, 69 [2] 143-148 (2013).

[26] J.P. Kelly and O.A. Graeve, "Spark Plasma Sintering as an Approach to the Manufacture of Bulk Materials: Feasibility and Cost Savings," *Journal of the Minerals*, 67 [1] 29-33 (2015).

[27] K. Sinha, B. Pearson, SR. Casolco, J.E. Garay, and O.A. Graeve, "Synthesis and Consolidation of $BaAl_2Si_2O_8$:Eu. Development of an Integrated Process for Luminescent Smart Ceramic Materials," *Journal of the American Ceramic Society*, 92 [11] 2504-2511 (2009).

[28] O.A. Graeve, R. Kanakala, L. Kaufman, K. Sinha, E. Wang, B. Pearson, G. Rojas-George, and J.C. Farmer, "Spark Plasma Sintering of Fe-Based Structural Amorphous Metals (SAM) with Y_2O_3 Nanoparticle Additions," *Materials Letters*, 62 [17-18] 2988-2991 (2008).

[29] JE. Garay, "Current-Activated Pressure-Assisted Densification of Materials" *The Annual Review of Materials Research*, 40, 445-468 (2010).

[30] JP. Kelly, OA. Graeve, "Spark Plasma Sintering as an Approach to Manufacture Bulk Materials: Feasibility and Cost Savings," *The Minerals, Metals & Materials Society*, 67 [1] 29-33 (2015).

[31] CEG. Bennett, NA. McKinnon, LS. Williams, "Sintering in gas discharges," *Nature*, 217, 1287-1289 (1968).

[32] K. Vanmeensel, A. Laptev, J. Hennicke, J. Vleugels, "Modelling of the temperature distribution during field assisted sintering," *Acta Materialia*, 53, 4379-4388 (2005).

[33] R. Chaim, "Densification mechanisms in spark plasma sintering of nanocrystalline ceramics," *Materials Science and Engineering a-Structural Materials Properties Microstructure and Processing*, 443, 25-32 (2007).

[34] M. Tokita, " Trends in advanced SPS spark plasma sintering systems and technology," *Journal of the Society of Powder Technology*, 30, 790-804 (1993).

[35] M. Tokita, "Development of hardware and software for," *J. High*, vol. 31, pp. 215-224, 2005.

[36] M. Tokita, " The potential of spark plasma sintering (SPS) method for the fabrication on an industrial scale of functionally graded materials," *Advances in Science and Technology*, 63, 322-331 (2010).

[37] ZA. Munir, U. Anselmi-Tamburini, M. Ohyanagi, " The effect of electric field and pressure on the synthesis and consolidation of materials: A review of the spark plasma sintering method," *Journal of Materials Science*, 41, 763-777 (2006).

[38] M. Tokita, "The potential of Spark Plasma Sintering (SPS) method for the fabrication on an industrial scale functionally graded material," *Advances in Science and Technology,* 63, 322-331 (2010).

[39] Y. Zhou, K.Hirao, M. Toriyama, "Very Rapid Densification of Nanometer Silicon Carbide Powder by Pulse Electric Current Sintering," *Journal of the American Ceramic Society*, 83, 654-656 (2000).

[40] U. Anselmi-Tamburini, JE. Garay, ZA Munir, A. Tacca, F. Maglia, G. Spinolo "Spark plasma sintering and characterization of bulk nanostructured fully stabilized zirconia: Part I. Densification studies," *Journal of Materials Research*, 19 [11] 3255-3262 (2004).

[41] XJ. Chen, KA. Khor, SH. Chan, LG. Yu, "Overcoming the effect of contaminant in solid oxide fuel cell (SOFC) electrolyte: spark plasma sintering (SPS) of 0.5 wt.% silica-doped yttria-stabilized zirconia (YSZ)" *Materials Science and Engineering: A*, 374, 64-71 (2004).

[42] SH. Risbud, JR. Groza, MJ. Kim, "Clean grain boundaries in aluminium nitride ceramics densified without additives by a plasma-activated sintering process," *Philosophical Magazine B*, 69, 525-533 (1994).

[43] ZA. Munir, U. Anselmi-Tamburini, "The effect of electric field and pressure on the synthesis and consolidation of materials: A review of the spark plasma sintering method" *Journal of Materials Science*, 41, 763-777 (2006).

[44] DE. Clark, WH. Sutton, "Microwave Processing of Materials," *Annual Review of Materials Science*, 26, 299-331 (1996).

[45] C. Musa, R. Licheri, A. Locci, R. Orru, "Energy efficiency during conventional and novel sintering processes: the case of Ti-Al2O3-TiC composites," *Journal of Cleaner Production*, 17, 877 (2009).

[46] C. Musa, R. Licheri, AM. Locci, R. Orrù, G. Cao, "Energy efficiency during conventional and novel sintering processes: the case of Ti-Al_2O_3-TiC composites," *Journal of Cleaner Production,* 17, 877-882 (2009).

[47] M. Tokita, "Development of Advanced Spark Plasma Sintering (SPS) systems and its industrial applications," *Pulse Electric Current Synthesis and Processing of Materials,* 51-59 (2006).

[48] J.M. Louin, L. Heraud, B. Malassine. Mechanical behavior of non-brittle ceramics: C-SiC and SiC-SiC composites. ICF7, Houston (USA). 1989.

[49] A. Noviyanto, Han YH, Yoon DH. Characteristics of SiCf/SiC hybrid composites fabricated by hot pressing and spark plasma sintering. Advances in Applied Ceramics, 110 [7]: 375-381 (2011).

[50] S. Schmidt, S. Beyer, H. Knabe, H. Immich, R. Meistring, A. Gessler. Advanced ceramic matrix composite materials for current and future propulsion technology applications. Acta Astronautica. 2004, 55: 409–420.

[51] H. Ohnabe, S. Masaki, M. Onozuka. Potential application of ceramic matrix composites to aero-engine components. Composites: Part A. 1999, 30: 489–496.

[52] F. Christin. Design, fabrication, and application of thermostructural composites (TSK) like C/C, C/SiC and SiC/SiC composites. Advanced Engineering Materials. 2000, 12: 903-912.

[53] R. Naslain. SiC-Matrix Composites: Nonbrittle Ceramics for Thermo Structural Application. International Journal of Applied Ceramic Technology. 2005, 2 [2]: 75–84.

[54] E. Novitskaya, H.E. Khalifa, O.A. Graeve. Microhardness and microstructure correlations in SiC/SiC composites. Materials Letters. 2018, 213: 286–289.

[55] R.E. Tressler. Recent developments in fibers and interphases for high temperature ceramic matrix composites. Composites Part A: Applied Science and Manufacturing. 1999, 30: 429-437.

[56] M. Suzuki, Y. Tanaka, Y. Inoue, N. Miyamoto, M. Sato K. Goda. Uniformization of boron nitride coating thickness by continuous chemical vapor deposition process for interphase of SiC/SiC composites. Journal of the Ceramic Society of Japan. 2003, 111 [12]: 865–871.

[57] R. Naslain. Design, preparation and properties of non-oxide CMCs for application in engines and nuclear reactors: an overview. Composites Science and Technology. 2004, 64: 155–170.

[58] R. Naslain, J.Y. Rossignol, P. Hagenmuller, F. Christin, L. Heraud, J.J. Choury. Influence of forced convection on the microstructure of "in situ" composites developed by controlled solidification. Revue de chimie minérale. 1981, 18: 544–564.

[59] L.V. Interrente, C.W. Whitmarsh, W. Sherwood. Fabrication of SiC matrix composites using a liquid polycarbosilane as the matrix source. Ceramic Transactions. 1995, 58: 111–118.

[60] N. Tamari, T. Tanaka, K. Takana. Effect of Spark Plasma Sintering on Densification and Mechanical properties of Silicon Carbide. Journal of the Ceramic Society of Japan. 1995, 108 [7]: 740-742.

[61] M. Tokita. Development of Advanced Spark Plasma Sintering (SPS) systems and its industrial applications. American Ceramic Society. 2006, 11: 314-316.

[62] J.E. Hensley, S.H. Risbud. Groza JR, Yamazaki K. Plasma-Activated Sintering of Aluminum Nitride. Journal of Materials Engineering and Performance. 1993, 2 [5]: 665-669.

[63] K. Yoshida, M. Imai, T. Yano. Processing and microstructure of silicon carbide fiber-reinforced silicon carbide composite by hot-pressing. Journal of Nuclear Materials. 1998, 258: 1960-1965.

[64] R. Naslain, "Fiber-Matrix Interphases and Interfaces in Ceramic Matrix Composites processed by CVI," *Composite Interfaces,* 3 [1] 253-286 (1993).

[65] C. Droillard, J. Lamon, "Fracture Toughness of 2D Woven SiC/SiC CVI Composites with Multilayered Interphases," *Journal of the American Ceramic Society,* 79 [4] 849-858 (1996).

[66] S. Pasquier, J. Lamon, R. Naslain, "Tensile Static Fatigue of 2D SiC/SiC Composites with Multilayered (PyC–SiC)N Interphases at High Temperatures in Oxidizing Atmosphere," *Composites Part A: Applied Science and Manufacturing,* 29, 1157-1164 (1998).

[67] C. Droillard, J. Lamon, X. Bourrat, "Strong Interface in CMCs, a Condition fo Efficient Multilayered Intherphases," *MRS Online Proceedings Library Archive,* 365, 371-376 (1994).

[68] JJ. Brennan, G. McCarthy, " Interfacial studies of refractory glass-ceramic-matrix/advanced-SiC-fiber-reinforced composites," *Materials Science and Engineering: A,* 162 [2] 53-72 (1993).

[69] RE. Jones, D. Petrak, J. Rabe, A. Szweda, "SYLRAMIC SiC fibers for CMC reinforcement," *Journal of nuclear materials,* 283, 556-559 (2000).

[70] RE. Tressler, "Recent developments in fibers and interphases for high temperature ceramic matrix composites," *Composites Part A: Applied Science and Manufacturing,* 30, 429-437 (1999).

[71] W. Krenkel, “Ceramic matrix composites: fiber reinforced ceramics and their applications,” (Wiley-VCH: New York, 2008).

[72] P. Fenici, AJF. Rebelo, RH. Jones, A. Kohyama, "Current status of SiC/SiC composites R & D.," *Journal of Nuclear Materials,* 258, 215-225 (1998).

[73] DB. Marshall, BN. Cox, AG. Evans, "The Mechanics of Matrix cracking in brittle-matrix fiber composites.," *Acta metallurgica,* 33, 2013-2021 (1985).

[74] K. Yoshida, "Development of silicon carbide fiber reinforced silicon carbide matrix composites with high performance based on interfacial and microstructure control .," *Journal of the Ceramic Society of Japan,* 118 [2] 82-90 (2010).

[75] AR. Bunsell, A. Piant, "A review of the development of the three generations of small diameter silicon carbide fibers.," *Journal of Materials Science,* 41, 823-839 (2006).

[76] A. Kohyama, M. Kotani, Y. Katoh, T. Nakayasu, "High-performance SiC/SiC composites by improved PIP processing with new precursor polymers," *Journal of Nuclear Materials,* 283, 565-569 (2000).

[77] JJ. Brennan, "Interfacial characterization of a slurry-cast melt-infiltrated SiC/SiC ceramic-matrix composite.," *Acta materialia,* 48, 4619-4628 (2000).

[78] E. Fitzer, A. Gkogkidis, " Carbon-Fiber-Reinforced Carbon Composites Fabricated by Liquid Impregnation," *ACS Symposium Series,* 303, 346-379 (1986).

[79] K. Yoshida, M. Imai, T. Yano, "Processing and microstructure of silicon carbide fiber-reinforced silicon carbide composite by hot-pressing.," *Journal of nuclear materials,* 258, 1960-1965 (1998).

[80] JB. Wachtman, WR. Cannon, MJ. Matthewson, "Mechanical Properties of Ceramics," (John Wiley & Sons, Inc./ Hoboken, NJ: 2nd ed., 2009).

[81] C. Hays, EG. Kendall, "An analysis of Knoop microhardness," *Metallography,* 28 [4] 1257-1262 (1973).

[82] D. Green, "An Introduction to the Mechanical Properties of Ceramics," (Cambridge University Press/ Cambridge, England 1998).

[83] TR. Simes, SG. Mellor, DA. Hills, " A note on the influence of residual stress on measured hardness," *The Journal of Strain Analysis for Engineering Design,* 19 [2] 135-137 (1984).

[84] SS. Chiang, DB. Marshall, AG. Evans, " The response of solids to elastic/plastic indentation. I. Stresses and residual stresses," *Journal of Applied Physics,* 53 [1] 298-311 (1982).

[85] ASTM International, "Standard Test Method for Knoop Indentation Hardness of Advanced Ceramics," (ASTM Standard C 1326-08E1/West Conshohocken, PA, 2008).

[86] Y. Milman, A. Golubenko. "Indentation size effect in nanohardness," *Acta Materialia,* 59, 7480–7487 (2011).

[87] A.Krell, "A new look at the influence of load, grain size and grain boundaries on teh room temperature hardness of ceramics," *International Journal of refractory Metals and Hard materials,* 16, 331-335 (1998).

[88] JP. Schaffer, A. Saxena, SD. Antolovich, TH. Sanders, “Science and Design of Engineering Materials,” (McGraw-Hil/ New York, NY, 2000).

[89] ASTM International, “Standard Test Method for Vickers Indentation Hardness of Advanced Ceramics,” (ASTM Standard C 1327-03/West Conshohocken, PA, 2003).

[90] B. &. Johnston, Mechanics of Materials (5th ed.), (McGraw-Hill Higher Education/New York,NY, 2006).

[91] NE. Dowling, “Mechanical behavior of materials: engineering methods for deformation, fracture, and fatigue, 3rd Edition,” (Prentice Hall/Upper Saddle River, NJ, 2007).

[92] ASTM International, “Standard Test Method for Flexural Strength of Advanced Ceramics at Ambient Temperature,” (ASTM Standard C 1161-02c /West Conshohocken, PA, 2008).

[93] Data provided by Ube Industries, Ltd.

[94] ASTM International, “Standard Test Method for Flexural properties of Continuous Fiber-Reinforced Advanced Ceramic Composites,” (ASTM Standard C 1341-13c /West Conshohocken, PA, 2013).

[95] KS. Mazdiyasni, “Fiber Reinforced Ceramic Composites: materials, processing and technology,” (Noyes Publications/ Park Ridge, New Jersey, 1990).

[96] Y. Tsung-Shou, MD. Sacks. "Effect of particle size distribution on the sintering of alumina," *Journal of the American Ceramic Society*, 71, 12 (1988).

[97] JR Groza, RJ. Dowding, “Nanoparticulate materials densification,” *Nanostructured Materials*, 7 [7] 749-768 (1996).

[98] M.Tokita, "Recent and Future Progress on Advanced Ceramics Sintering by Spark Plasma Sintering," *Nanotechnologies in Russia,* 10 [3] 261-267 (2015).

[99] A. Noviyanto, YH. Han, DH. Yoon, " Characteristics of SiCf/SiC hybrid composites fabricated by hot pressing and spark plasma sintering," *Advances in Applied Ceramics,* 110 [7] 375-381 (2011).

[100] Y. Ding, S. Dong, Q. Zhou. Preparation of C/SiC Composites by Hot Pressing, Using Different C Fiber Content as Reinforcement. Journal of American Ceramic Society. 2006, 89 [4]: 1447–1449.

[101] J.L Cabezas, L. Olmos. Investigation of the effect of inert inclusions on densification during solid-state sintering of metal matrix composites. Science and Engineering of Composite Materials. 2017, 24 [5]: 755-763.

[102] K. Shimoda, A. Kohyama, T. Honiki. High mechanical performance SiC/SiC composites by NITE process with tailoring of appropriate fabrication temperature to fiber volume fraction. Composites Science and Technology. 2009, 69: 1623-1628.

[103] M.Tokita, “Trends in advanced SPS spark plasma sintering systems and technology,” *Journal of the Society of Powder Technology, Japan*, 30, 790-804 (1993).

[104] O. Guillon, J. Gonzalez-Julian, B. Dargatz, “Field-Assisted Sintering Technology/Spark Plasma Sintering: Mechanisms, Materials and Technology Developments” *Advanced Engineering Materials*, 16 [7] 830-849 (2014).

[105] Zhang T, Qi L, Li S. Effect of PyC coating on mechanical properties of Cf/AZ91D composites. *Surface Engineering*. 2017; 1-9.

[106] ST. Gonczy, MG. Jenkins, "Flexure Testing of Nicalon™ 2-D Fiber Reinforced Sylramic™ S-200 Ceramic Composites— A Multilaboratory Round Robin Test," Annual Conference on Composites, Advanced Ceramics, Materials, and Structures: A: Ceramic Engineering and Science Proceedings, 20 [3] 615-623 (1999).

[107] FI. Baratta, WT. Matthews, GD. Quinn, "Errors Associated with Flexure Testing of Brittle Materials," *U.S. Army Materials Technology Lab Report MTL TR,* 2, 87-105 (1987).

[108] Y. Zhou, F. Pervin, S. Jeelani, PK. Mallick, "Improvement in mechanical properties of carbon fabric epoxy composite using carbon nanofibers," *Journal of Materials Processing Technology*, 198, 445-453 (2008).

[109] JL. Abot, Y. Song, MJ. Schulz, VN. Shanov, "Novel carbon nanotube array-reinforced laminated composite materials with higher interlaminar elastic properties," *Composites Science and Technology,* 68, 2755-2760 (2008).

[110] M. Jacob, S. Thomas, KT. Varughese, "Mechanical properties of sisal/oil palm hybrid fiber reinforced natural rubber composites," *Composites Science and Technology,* 64, 955-965 (2004).

[111] R. Velmurugan, V. Manikandan, "Mechanical properties of palmyra/glass fiber hybrid composites," *Composites Part A: applied science and manufacturing*, 38, 2216-2226 (2007).

[112] Aveston, J. , G. A Cooper, A Kelly. Single and Multiple Fracture, The Properties of Fibre composites Conference Proceedings, IPC Science and Technology Press Guilford, UK 1971

[113] S. Guptaa, S. Kumar Sharmaa, B. Venkata Manoj Kumara, Y.W. Kim. Tribological characteristics of SiC ceramics sintered with a small amount of yttria. Ceramics International. 2015, 41; 14780-14789.

[114] P. Klimczyk. SiC-based composites sintered with high pressure method. In Silicon carbide-materials, processing and applications in electronic devices. 2011.

[115] Pujar VV, Cawley JD. Effect of Stacking Faults on the X-ray Diffraction Profiles of β-SiC Powders. *Journal of the American Ceramic Society*. 1995; 78: 774-782.

[116] Pujar VV, Cawley JD. Computer Simulations of Diffraction Effects due to Stacking Faults in β-SiC: II, Experimental Verification. *Journal of the American Ceramic Society*. 2001; 84 [11]: 2645-2651.

[117] Shinoda Y. Fabrication of nanograined silicon carbide by ultrahigh pressure hot isostatic pressing. *Journal of the American Ceramic Society*.1999; 82: 771-773.

[118] Uvarov V, Popov I. Development and metrological characterization of quantitative X-ray diffraction phase analysis for the mixtures of clopidogrel bisulphate polymorphs. *Journal of Pharmaceutical and Biomedical Analysis*. 2008; 46: 676–682.

[119] Roberts SN, Williams AC, Grimsey IM, Booth SW. Quantitative analysis of mannitol polymorphs. X-ray powder diffractometry-exploring preferred orientation effects. *Journal of Pharmaceutical and Biomedical Analysis*. 2002; 28: 1149–1159.

[120] Qiu J, Li G, Sheng Y, Zhu M. Quantification of febuxostat polymorphs using powder X-ray diffraction technique. *Journal of Pharmaceutical and Biomedical Analysis*. 2015; 107: 298–303.

[121] Mulla MA, Krstic VD. Low-Temperature Pressureless Sintering of β-SiC with Alumina and Yttrium Oxide Additions. *American Ceramic Society Bulletin*. 1991; 70 [3]: 439–443.

[122] Powell JA, Herbert W. Low-temperature solid-state phase transformations in 2H silicon carbide. *Journal of Applied Physics*. 1972; 43 [4]: 1400-1408.